

Electronic Supplementary Information

Boosting Structural Variety and Catalytic Activity of Porphyrinic Metal-Organic Frameworks by Harnessing Bifunctional Ligand

Wei Wu,^a Xiu-Liang Lv,^{*,a} Tao He,^a Guang-Rui Si,^a Hongliang Huang,^b Lin-Hua Xie,^{*,a} Yabo Xie,^a and Jian-Rong Li^a

^a Beijing Key Laboratory for Green Catalysis and Separation, Department of Chemical Engineering
Beijing University of Technology
Beijing, 100124 (P. R. China)

^b State Key Laboratory of Separation Membranes and Membrane Processes, School of Chemistry and
Chemical Engineering
Tiangong University
Tianjin 300387 (P. R. China)

E-mail: lvxiuliang@bjut.edu.cn; xielinhua@bjut.edu.cn

Table of Contents

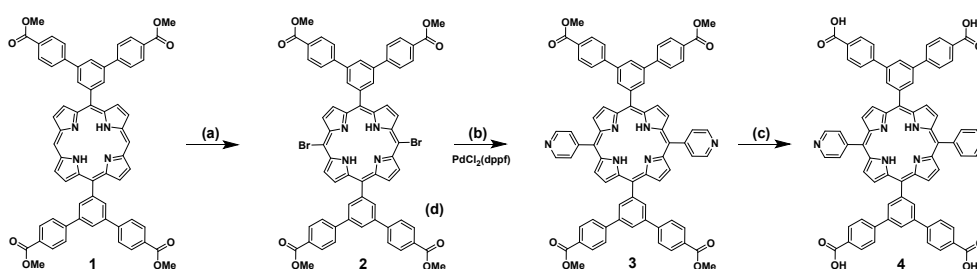
S1. Materials and instruments.....	3
S2. Ligand Synthesis.....	3
S3. MOF Synthesis	7
S4. Single-Crystal X-ray Crystallography	8
S5. Structural Illustration	10
S6. Inductively Coupled Plasma-Atomic Emission Spectrometry (ICP-AES)	13
S7. Powder X-ray Diffraction.....	14
S8. N ₂ Sorption Isotherms.....	19
S9. Thermogravimetric Analysis (TGA)	22
S10. Fourier Transform Infrared Spectrometer Spectra (FT-IR).....	24
S11. Liquid-phase Adsorption	25
S12. UV-vis/photoluminescence and electrochemical measurements.....	27
S13. DFT calculations for the HOMO and LUMO of ligands	32
S14. Electron Paramagnetic Resonance (EPR) Spectroscopy	33
S15. Photocatalysis Data.....	34
S16. References.....	42

S1. Materials and instruments

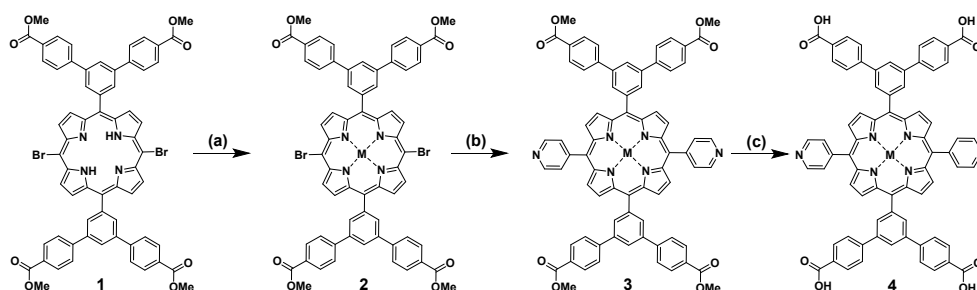
All reagents and solvents were purchased commercially and used directly without further purification. ^1H NMR data were measured on BRUKER AVANCE III HD 400 MHz spectrometer. Thermogravimetry analysis (TGA) data were obtained on a TGA-50 (SHIMADZU) thermogravimetric analyzer under the air atmosphere with a heating rate of $10\text{ }^\circ\text{C min}^{-1}$. The powder X-ray diffraction (PXRD) patterns were performed on the Rigaku Smartlab3 X-ray Powder diffractometer equipped with a Cu sealed tube ($\lambda = 1.54178\text{ \AA}$) at room temperature. N_2 adsorption/desorption isotherms were measured on a Micromeritics ASAP 2020 physisorption analyzer at 77 K.

S2. Ligand Synthesis

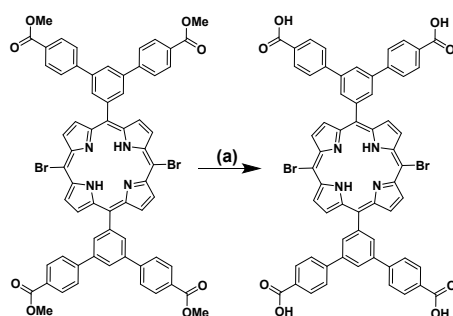
BBCPPP, L-Ph, and L-Py were synthesized according to our previous article.¹ Other metal-involved **M-L-Py** ligands ($\text{M} = \text{Fe(III)}, \text{Ni(II)}, \text{Cu(II)}$) were synthesized by three steps as Scheme S2. The TCPP ligand (tetrakis(4-carboxyphenyl)porphyrin) was synthesized based on previous reports with slight modifications.²



Scheme S1. Synthetic procedure for **L-Py**: (a) NBS, CH_2Cl_2 ; (b) K_2CO_3 , pyridine-4-boronic acid, $\text{PdCl}_2(\text{dppf})$, dioxane, H_2O , $100\text{ }^\circ\text{C}$; (c) NaOH, THF, CH_3OH , H_2O , $70\text{ }^\circ\text{C}$.



Scheme S2. Synthetic procedure for **M-L-Py**: (a) DMF, metal salt ($\text{FeCl}_2 \cdot 4\text{H}_2\text{O}$, $\text{NiCl}_2 \cdot 6\text{H}_2\text{O}$, $\text{CuCl}_2 \cdot 2\text{H}_2\text{O}$), $150\text{ }^\circ\text{C}$; (b) K_2CO_3 , pyridine-4-boronic acid, $\text{PdCl}_2(\text{dppf})$, dioxane, H_2O , $100\text{ }^\circ\text{C}$; (c) NaOH, THF, CH_3OH , H_2O , $70\text{ }^\circ\text{C}$.



Scheme S3. Synthetic procedure for **L-Br**: (a) NaOH, THF, CH_3OH , H_2O , $70\text{ }^\circ\text{C}$.

5',5''-(10,20-dibromoporphyrin-5,15-diyl)bis([1,1':3',1''-terphenyl]-4,4''-dicarboxylate) (L-Br). Tetramethyl 5',5''-(10,20-dibromoporphyrin-5,15-diyl)bis([1,1':3',1''-terphenyl]-4,4''-dicarboxylate)¹ (1.0 g, 0.86 mmol) and 2 M NaOH (30 mL) were suspended in THF (30 mL) and CH₃OH (30 mL). The mixture was stirred at 70 °C overnight. When the reaction was complete, THF and CH₃OH were removed by distillation under reduced pressure. The obtained aqueous phase was adjusted to pH = 3 by adding concentrated HCl. The precipitate was filtered, washed with water (200 mL × 3), ethanol (200 mL × 3), and acetone (200 mL × 3), then dried at 80 °C to afford 5',5''-(10,20-dibromoporphyrin-5,15-diyl)bis([1,1':3',1''-terphenyl]-4,4''-dicarboxylate) (L-Br) as the purple solid (0.84 g, 0.76 mmol, 88.28%). ¹H NMR (DMSO-*d*₆, 400 MHz): δ = 13.08 (s, 4H), 9.71 (s, 4H), 9.05 (s, 4H), 8.63 (d, *J* = 16 Hz, 6H), 8.23 (d, *J* = 8 Hz, 8H), 8.10 (d, *J* = 8 Hz, 8H), -2.91 (s, 2H).

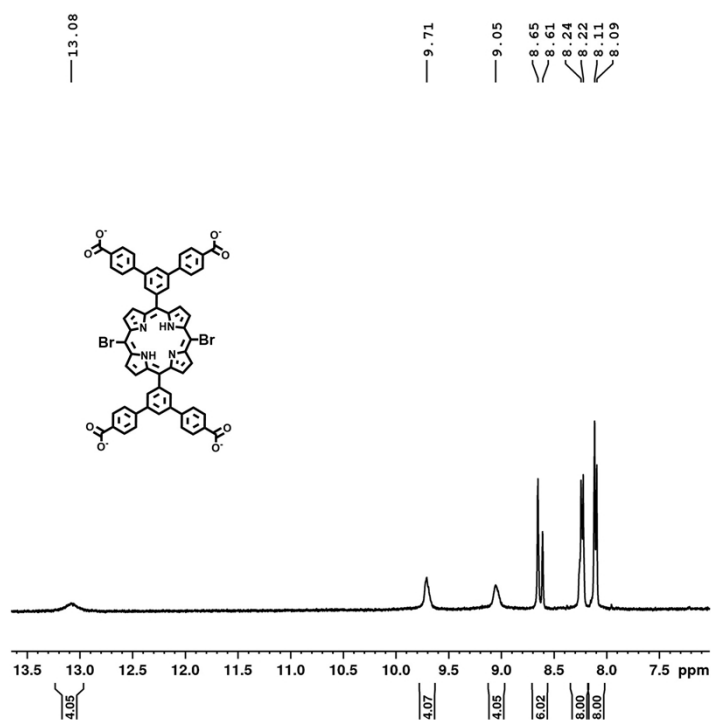


Figure S1. ¹H NMR (DMSO-*d*₆, 400 MHz) spectrum of L-Br.

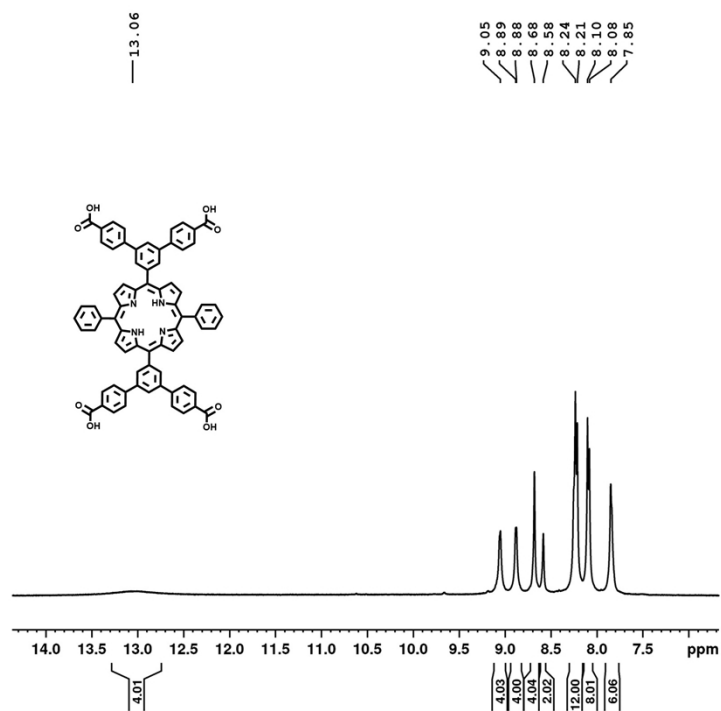


Figure S2. $^1\text{H NMR}$ (DMSO- d_6 , 400 MHz) spectrum of L-Ph.

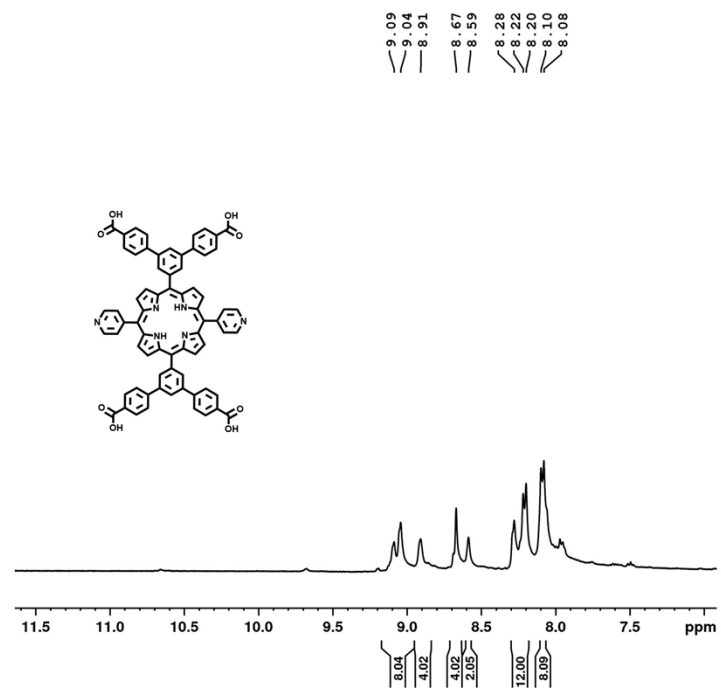


Figure S3. $^1\text{H NMR}$ (DMSO- d_6 , 400 MHz) spectrum of L-Py.

5,10,15,20-Tetrakis(4-methoxycarbonylphenyl)porphyrin (TPPCOOMe).

The methyl *p*-formylbenzoate (6.9 g, 42 mmol) was dissolved in propionic acid (100 mL). Then pyrrole was added dropwise (3.0 mL, 0.043 mol), and the solution was refluxed for 12 h in darkness. After the reaction, the mixture was cooled to room temperature, and the precipitates were collected by filtration, washed with methanol, and dried in a vacuum oven (1.9 g, 21 %).

Tetrakis(4-carboxyphenyl)porphyrin (TCPP).

The obtained ester (1 g) and 2 M NaOH (30 mL) were suspended in THF (30 mL) and CH₃OH (30 mL). The mixture was stirred at 70 °C overnight. When the reaction was complete, THF and CH₃OH were removed by distillation under reduced pressure. The obtained aqueous phase was adjusted to pH = 3 by adding concentrated HCl. The precipitate was filtered, washed with water (200 mL × 3), and dried at 80 °C to afford TCPP.

S3. MOF Synthesis

Synthesis of BUT-229 and BUT-229(M).

L-Py (4 mg, 0.0036 mmol), $ZrCl_4$ (10 mg, 0.043 mmol), and acetic acid (500 mL) were added to 2 mL of *N,N*-diethylformamide (DEF) in a 4 mL glass bottle and dissolved by sonication. The mixture was heated in a 120 °C oven for three days. After cooling down to room temperature, dark purple block crystals of BUT-229 were harvested (3.4 mg, 61% based on L-Py). Elemental analyses (EA): Anal. calc. for $C_{139}H_{76}N_{12}O_{32}Pd_{0.5}Zr_6$, C (55.16%), H (2.53%), N (5.55%); found C (55.31%), H (2.54%), N (5.53%). BUT-229(Fe)/BUT-229(Ni)/BUT-229(Cu) could be synthesized under the same condition using Fe-L-Py/Ni-L-Py/Cu-L-Py.

Synthesis of BUT-230 and BUT-230(M).

L-Py (4 mg, 0.0036 mmol), $ZrCl_4$ (10 mg, 0.043 mmol), and formic acid (0.2 mL) were added to 2 mL of *N,N*-diethylformamide (DEF) in a 4 mL glass bottle and dissolved by sonication. The mixture was heated in a 120 °C oven for three days. After cooling down to room temperature, dark purple block crystals of BUT-230 were harvested (3.7 mg, 67% based on L-Py). BUT-230(Fe)/BUT-230(Ni)/BUT-230(Cu) could be synthesized under the same condition using Fe-L-Py/Ni-L-Py/Cu-L-Py. Elemental analyses (EA): Anal. calc. for $C_{142}H_{74}N_{12}O_{32}Pd_{0.2}Zr_6$, C (56.31%), H (2.46%), N (5.55%); found C (56.46%), H (2.45%), N (5.56%).

Synthesis of BUT-231.

L-Br (4 mg, 0.0036 mmol), $ZrCl_4$ (10 mg, 0.043 mmol), and acetic acid (0.35 mL) were added to 2 mL of *N,N*-diethylformamide (DEF) in a 4 mL glass bottle and dissolved by sonication. The mixture was heated in a 120 °C oven for three days. After cooling down to room temperature, dark purple block crystals of BUT-231 were harvested (4.1 mg, 75% based on L-Br). Elemental analyses (EA): Anal. calc. for $C_{122}H_{58}N_8O_{32}Br_4Pd_{0.2}Zr_6$, C (48.27%), H (1.93%), N (3.69%); found C (48.34%), H (1.94%), N (3.68%).

Synthesis of BUT-232.

L-Ph (4 mg, 0.0036 mmol), $ZrCl_4$ (10 mg, 0.043 mmol), and benzoic acid (BA) (400 mg, 3.28 mmol) were added to 2 mL of *N,N*-diethylformamide (DEF) in a 4 mL glass bottle and dissolved by sonication. The mixture was heated in a 120 °C oven for three days. After cooling down to room temperature, dark red block crystals of BUT-232 were harvested (4.1 mg, 72% based on L-Ph). Elemental analyses (EA): Anal. calc. for $C_{146}H_{78}N_8O_{32}Pd_{0.2}Zr_6$, C (57.98%), H (2.60%), N (3.70%); found C (57.89%), H (2.59%), N (3.71%).

PCN-625³, PCN-222⁴, PCN-226⁵, and Al-PMOF⁶ were synthesized according to the previous literature with slight modifications.

Synthesis of PCN-625.

BBCPPP (4 mg), $ZrCl_4$ (10 mg), and formic acid (0.7 mL) were added to 2 mL of *N,N*-diethylformamide (DEF) in a 4 mL glass bottle and dissolved by sonication. The mixture was heated in a 120 °C oven for three days. After cooling down to room temperature, dark red block crystals of PCN-625 were harvested (yield: 75%).

Synthesis of PCN-222.

T CPP (12.5 mg), $ZrOCl_2 \cdot 8H_2O$ (23.5 mg), and 4-tert-Butylbenzoic acid (1350 mg) were added to 3 mL DEF in a 4 mL glass bottle and dissolved by sonication. The mixture was heated in a 120 °C oven for 12 h. After cooling down to room temperature, violet crystals of PCN-222 were harvested.

Synthesis of PCN-226.

T CPP (70 mg), $ZrCl_4$ (210 mg), and benzoic acid (7.0 g) were added to 14 mL DMF in a Teflon-lined steel-autoclave and dissolved by sonication. The mixture was heated in a 140 °C oven for 72 h. After cooling down to room temperature, violet needle-shaped crystals of PCN-226 were harvested.

Synthesis of Al-PMOF.

T CPP (100 mg) and $AlCl_3 \cdot 6H_2O$ (60 mg) were added to 10 mL deionized water in a Teflon-lined steel-autoclave and dissolved by sonication. The mixture was heated in a 180 °C oven for 16 h. After cooling down to room temperature, the red solid of PCN-226 were harvested.

Sample Activation

The MOFs were soaked in fresh DMF (20 mL) at 80 °C for 24 hours. Then the samples were soaked in fresh acetone (20 mL) for two days at room temperature (refreshing acetone every 12 hours). Before tests, the samples were loaded in a sample tube and further activated under a vacuum at 80 °C for 10 hours.

S4. Single-Crystal X-ray Crystallography

As-synthesized crystals were taken from the mother liquid, transferred to oil, and mounted onto a loop for single-crystal X-ray data collection. The crystals data of BUT-229, and BUT-232 were collected in a Rigaku Supernova CCDC diffractometer equipped with a mirror-monochromatic enhanced Cu-K α radiation ($\lambda = 1.54178 \text{ \AA}$) at 293 K. The datasets were corrected by empirical absorption correction using spherical harmonics, implemented in the SCALE3 ABSPACK scaling algorithm. The structures of the two MOFs were solved by direct methods and refined by full-matrix least-squares on F^2 with anisotropic displacement using the SHELXTL software package. All the non-hydrogen atoms on the frameworks were refined with anisotropic displacement parameters during the final cycles. All the hydrogen atoms of ligands were solved in ideal positions with isotropic displacement parameters. There are large pore volumes occupied by highly disordered solvent molecules in the frameworks of these MOFs. No satisfactory disorder model was used for solving these solvent molecules, so the SQUEEZE program implemented in PLATON was used to remove the electron densities of these disordered guests. The pyridyl groups and porphyrin core of L-Py ligand in BUT-229 are disordered at two positions all with half occupancy. Similar disorder of the ligand was also observed in BUT-232. Geometry constraint instructions were applied to the disordered parts of the ligands during the refinement cycles. Q peaks with moderate electron density were found at porphyrin ring centers of the ligands in BUT-229 and BUT-232, which were assigned to be Pd(II) atoms with partial occupancy. Their occupancies were refined freely until the final refinement cycles. The PXRD patterns of BUT-230/-231 are identical to the PXRD patterns of PCN-625 and BUT-232, indicating the isostructure of these MOFs (Figure S10). The details of crystal data and structure refinement are summarized in Table S1 and the CIF files (CCDC: 2265020, 2265021).

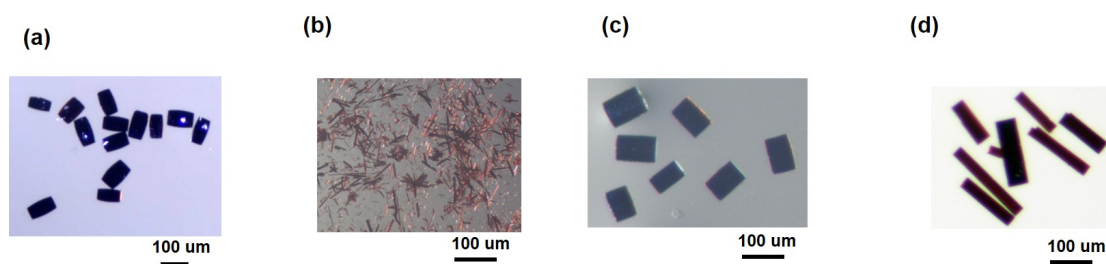


Figure S4. Optical photos for the crystals of (a) BUT-229, (b) BUT-230, (c) BUT-231 and (d) BUT-232.

Table S1. Crystallographic data for **BUT-229** and **BUT-232**

Compound name	BUT-229	BUT-232
Empirical formula	C ₁₃₉ H ₇₆ N ₁₂ O ₃₂ Pd _{0.5} Zr ₆	C ₁₄₆ H ₇₈ N ₈ O ₃₂ Pd _{0.2} Zr ₆
Formula weight	3026.63	3024.76
Temperature (K)	293(2)	293(2)
Crystal system	orthorhombic	hexagonal
Space group	<i>Fmmm</i>	<i>P6/mmm</i>
<i>a</i> (Å)	19.3571(8)	40.1656(8)
<i>b</i> (Å)	34.6876(7)	40.1656(8)
<i>c</i> (Å)	49.1146(8)	24.2320(7)
α /°	90	90
β /°	90	90
γ /°	90	120
<i>V</i> (Å ³)	32978.1(16)	33855.4(17)
<i>Z</i>	4	3
Calculated density (g/cm ³)	0.610	0.445
μ (mm ⁻¹)	1.986	1.357
<i>F</i> (000)	6052.0	4546.0
Reflections collected	20781	54575
Independent reflections	8472 [<i>R</i> _{int} = 0.0539, <i>R</i> _{sigma} = 0.0619]	12070 [<i>R</i> _{int} = 0.0755, <i>R</i> _{sigma} = 0.0689]
Data/restraints/parameters	8472/495/307	12070/531/340
Goodness-of-fit on <i>F</i> ²	0.998	0.994
Final <i>R</i> indexes [<i>I</i> > 2σ(<i>I</i>)]	<i>R</i> ₁ ^a = 0.0676, <i>wR</i> ₂ ^b = 0.1861	<i>R</i> ₁ = 0.0598, <i>wR</i> ₂ = 0.1686
Final <i>R</i> indexes [all data]	<i>R</i> ₁ = 0.1220, <i>wR</i> ₂ = 0.2304	<i>R</i> ₁ = 0.1104, <i>wR</i> ₂ = 0.2014
Largest diff. peak/hole (e/Å ³)	0.93/-0.60	1.30/-0.76

^a $R_1 = \sum ||F_o| - |F_c|| / \sum |F_o|$. ^b $wR_2 = [\sum w(F_o^2 - F_c^2)^2 / \sum w(F_o^2)^2]^{1/2}$

S5. Structural Illustration

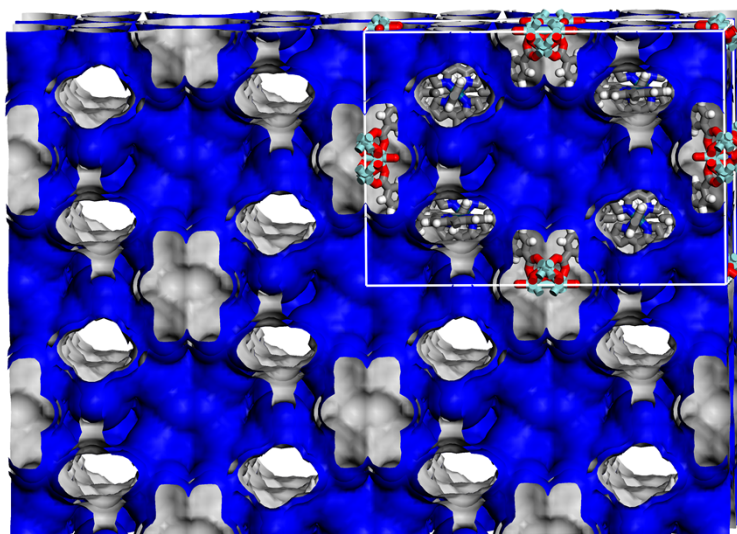


Figure S5. Three-dimensional pore system in BUT-229 view along the *a* axis (the external and internal pore surfaces are shown in gray and blue, respectively; probe radius = 1.0 Å).

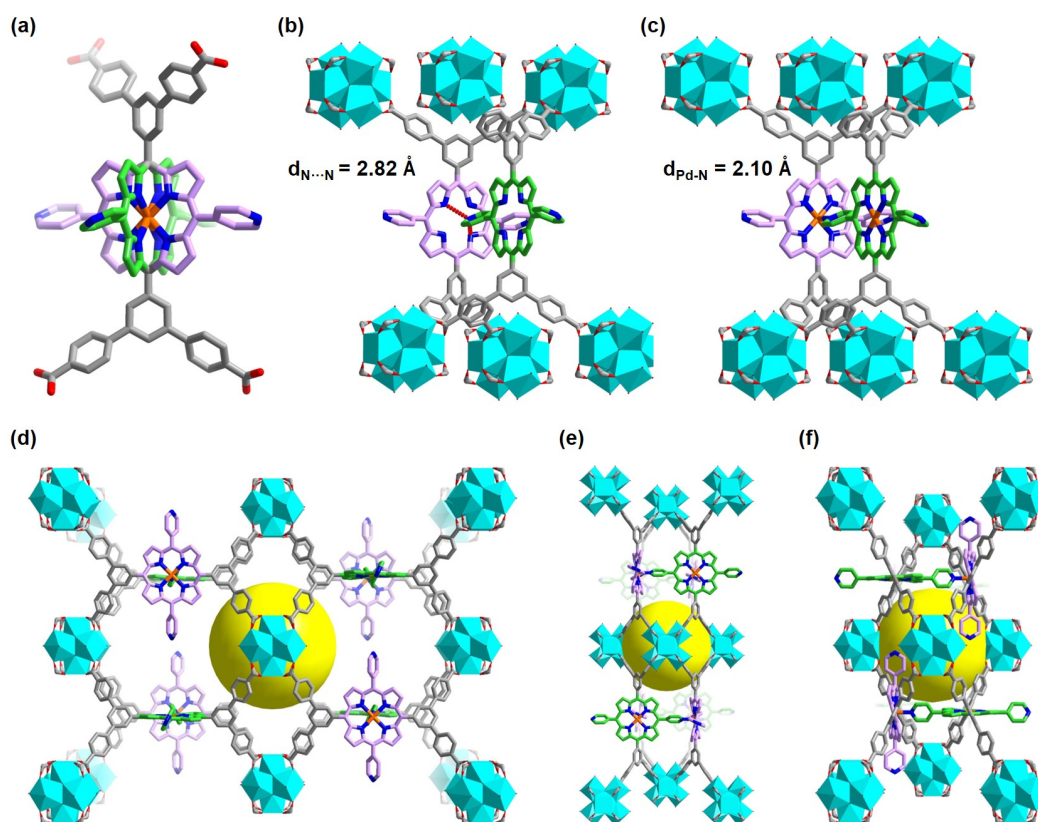


Figure S6. Structural illustration of BUT-229. (a) The ligand in BUT-229 disordered at two positions with C-C and C-N bonds in the two disordered part highlighted in green and pink, respectively. (b) The hydrogen bonding interaction between pyridine group and neighbouring porphyrin ring. (c) The coordination of pyridine group with Pd(II) center in neighbouring porphyrin ring. The crystal structure of BUT-229 after manual removal of the disorder view along the (d) *a*-axis, (e) *b*-axis, and (f) *c*-axis (yellow sphere stands for the pore space).

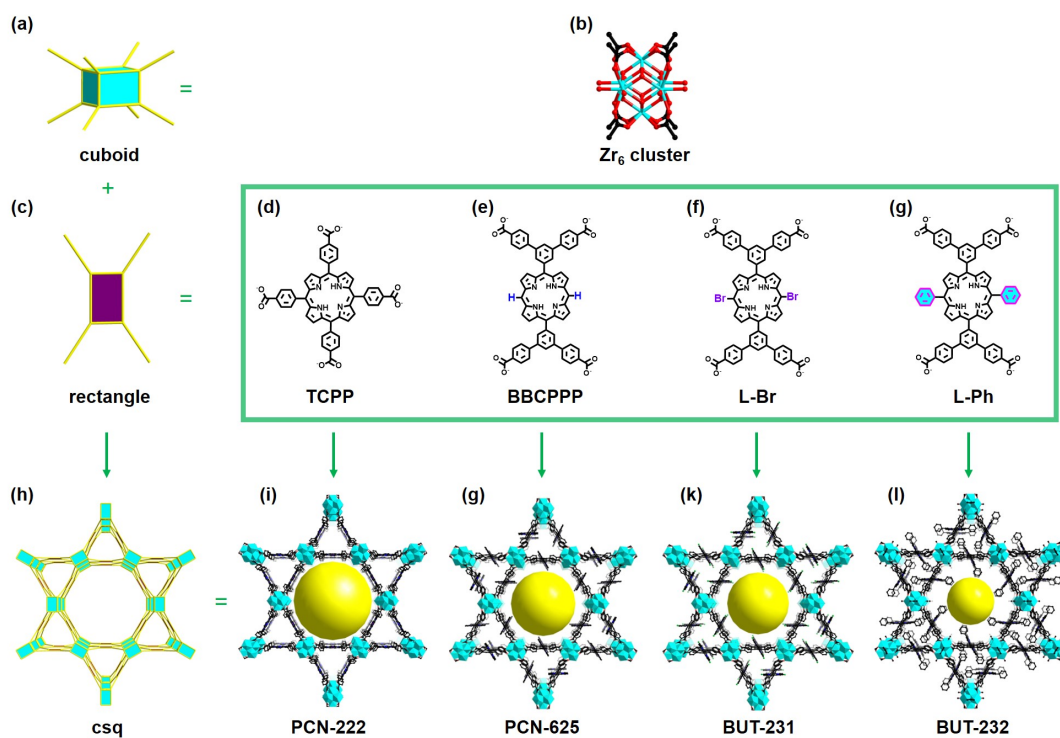


Figure S7. Construction of the Zr-PMOFs with *csq* topology. (a, b) 8-connected Zr_6 clusters. (c) The rectangle configuration. (d-g) Different ligands of TCPP, BBCPPP, L-Br, and L-Ph. (h) *csq* topology. (i-l) The framework structures of PCN-222, PCN-625, BUT-231 and -232.

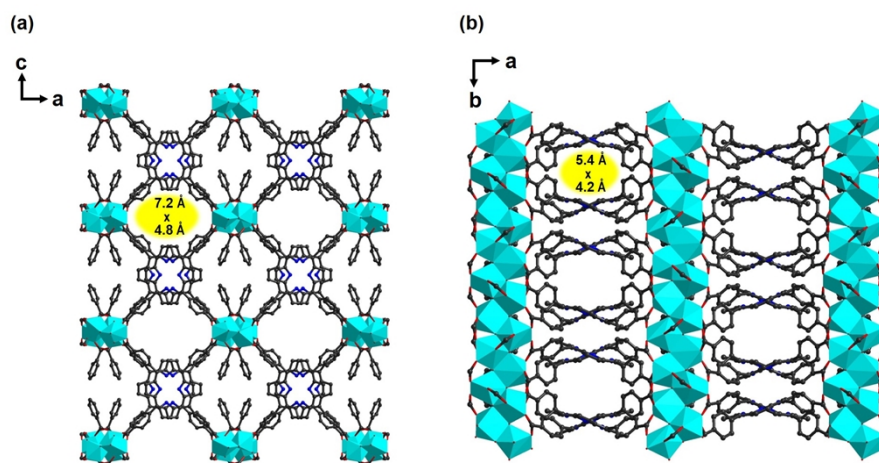


Figure S8. The crystal structure of PCN-226 viewed along the (a) *b*-axis and the (b) *c*-axis.

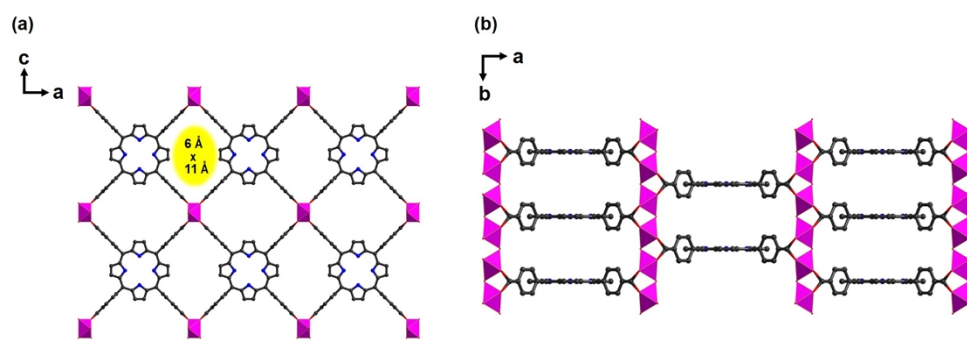


Figure S9. The crystal structure of Al-PMOF viewed along the (a) b -axis and the (b) c -axis.

S6. Inductively Coupled Plasma-Atomic Emission Spectrometry (ICP-AES)

The activated MOFs (10 mg for each) were treated with concentrated nitric acid (65%), and the mixtures were heated at 150 °C in the autoclave for 24 h. The resulting solutions were diluted with deionized water to a concentration of around 10 ppm before ICP testing.

Table S2. ICP-AES data of the activated MOFs (data presented in the table were obtained by averaging the results of three independent measurements).

Sample name	Zr (mg/L)	Pd (mg/L)	Zr/Pd (n/n)
BUT-229	12.04	0.47	29.88
BUT-230	17.64	0.69	29.82
BUT-232	13.24	0.52	29.70

S7. Powder X-ray Diffraction

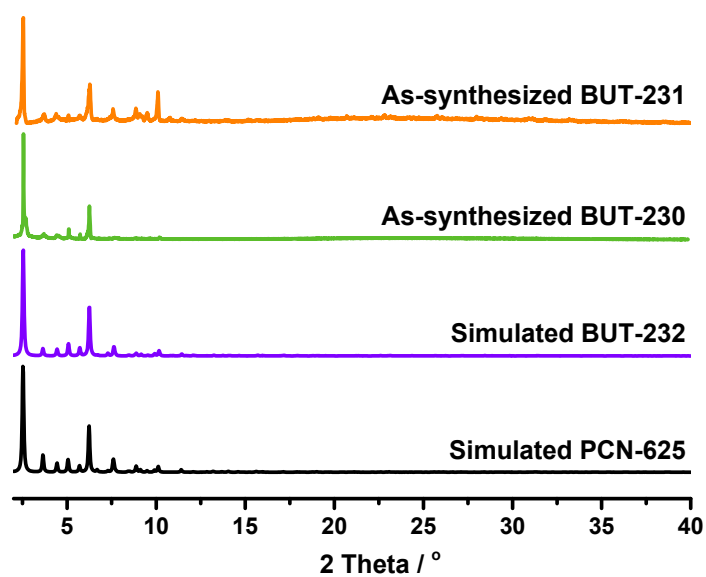


Figure S10. PXRD patterns of as-synthesized BUT-230/-231 and simulated PCN-625 and BUT-232.

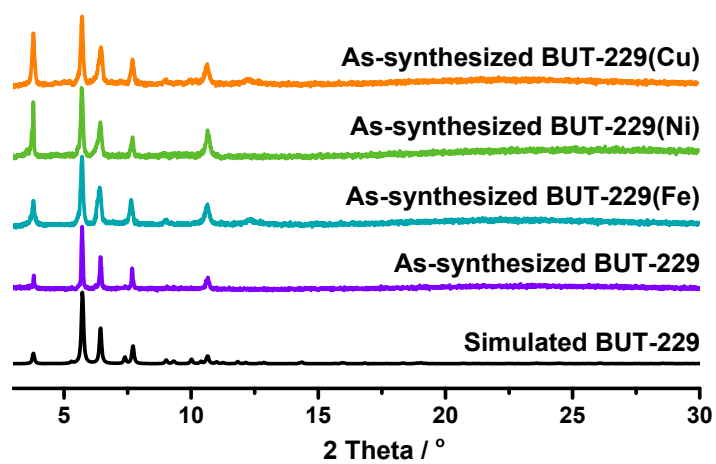


Figure S11. PXRD patterns of as-synthesized BUT-229, BUT-229(Fe), BUT-229(Ni), and BUT-229(Cu).

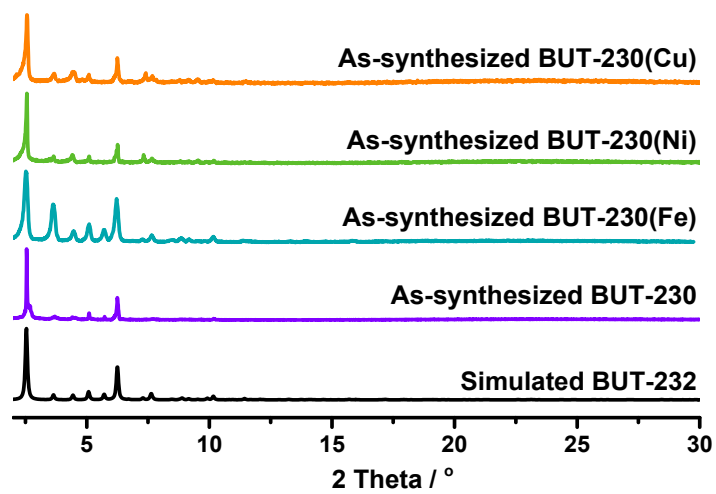


Figure S12. PXRD patterns of as-synthesized BUT-230, BUT-230(Fe), BUT-230(Ni), and BUT-230(Cu).

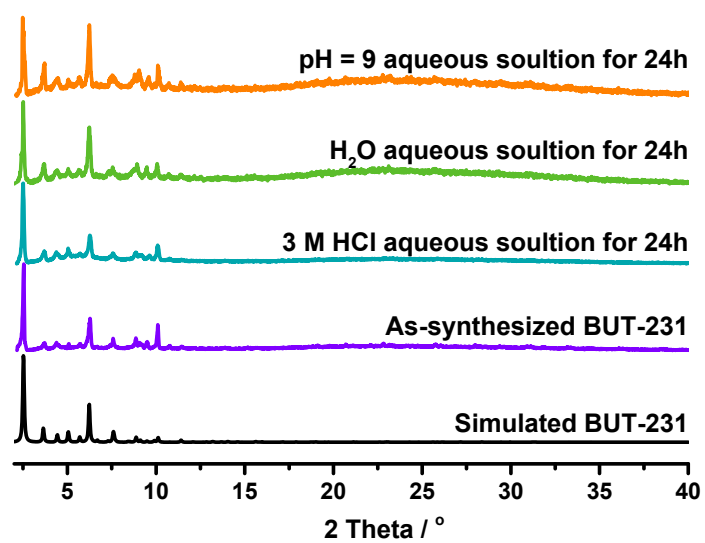


Figure S13. PXRD patterns of BUT-231 samples after being treated in different conditions.

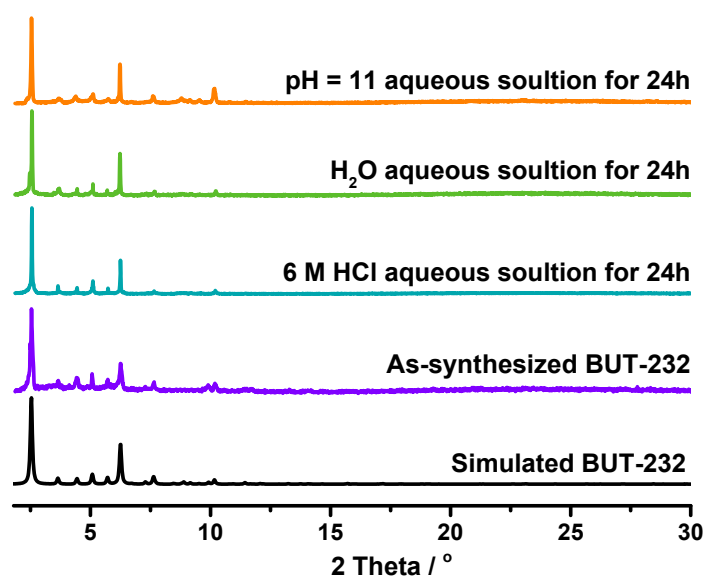


Figure S14. PXRD patterns of BUT-232 samples after being treated in different conditions.

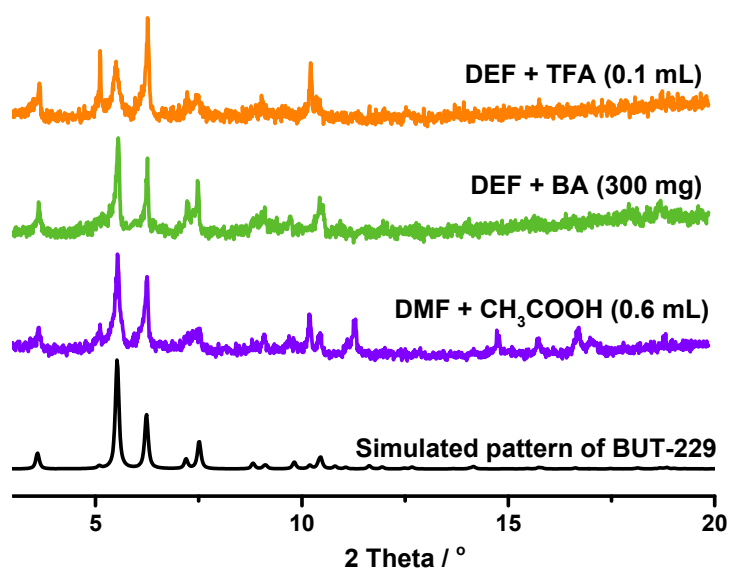


Figure S15. PXRD patterns of the products from the reactions between L-Py and $ZrCl_4$ in DMF or DEF with different modulators. BA: benzoic acid; TFA: trifluoroacetic acid.

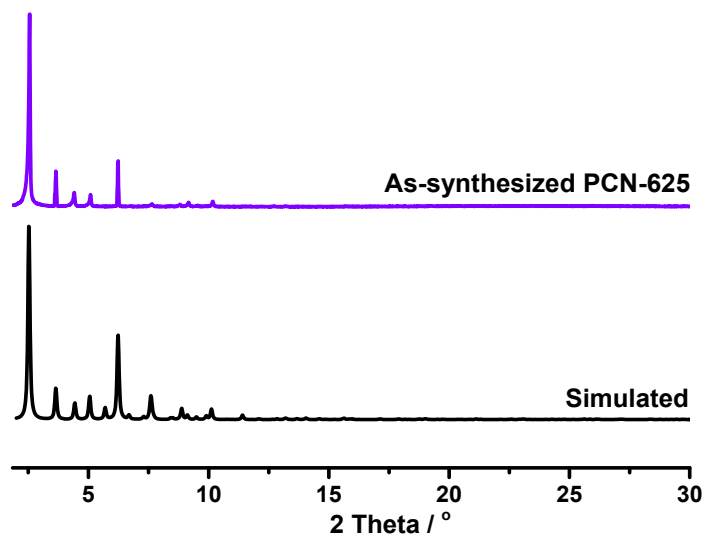


Figure S16. PXRD patterns of PCN-625.

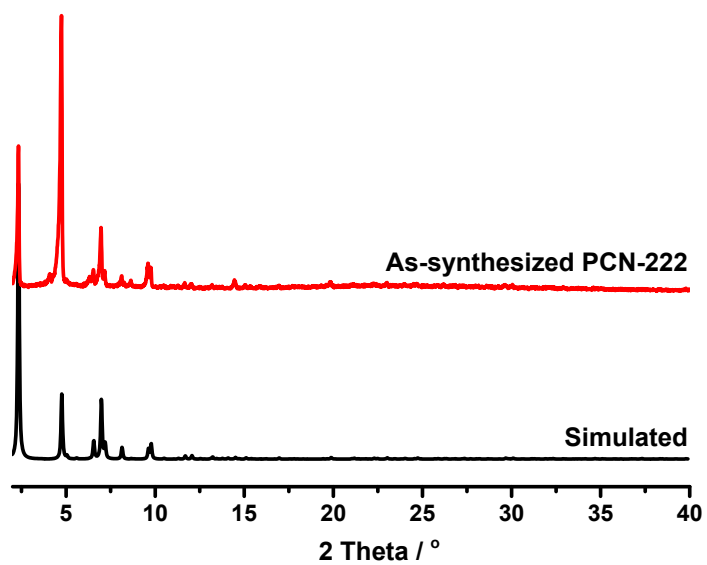


Figure S17. PXRD patterns of PCN-222.

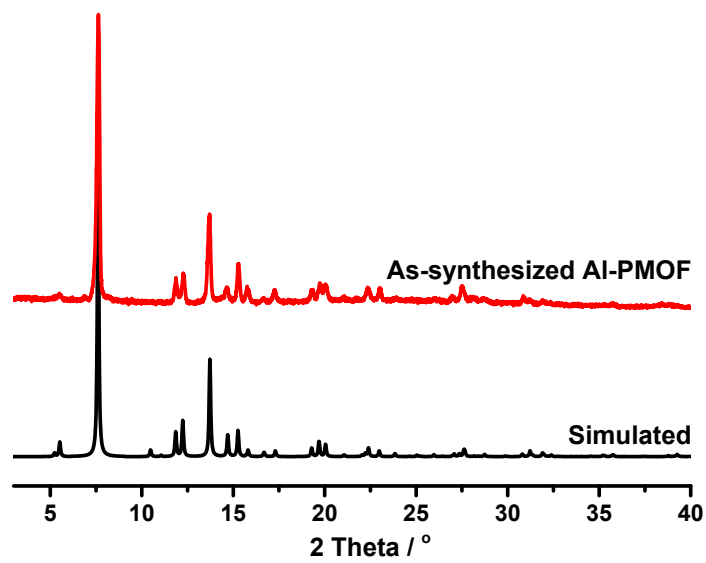


Figure S18. PXRD patterns of Al-PMOF.

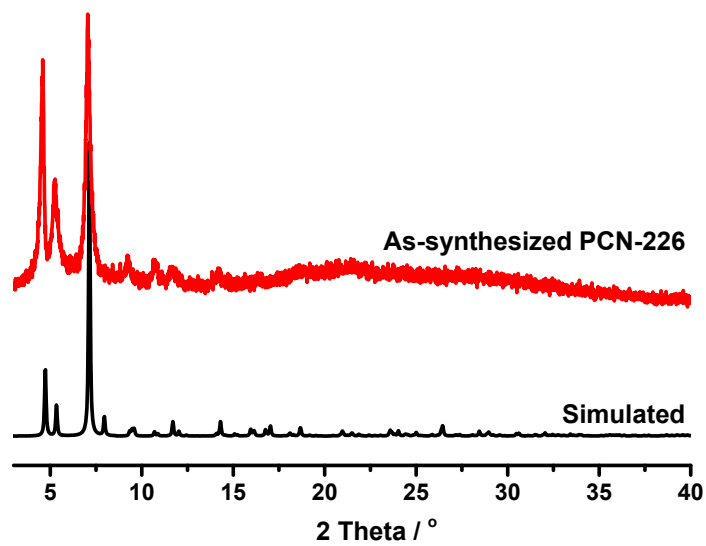


Figure S19. PXRD patterns of PCN-226.

S8. N₂ Sorption Isotherms

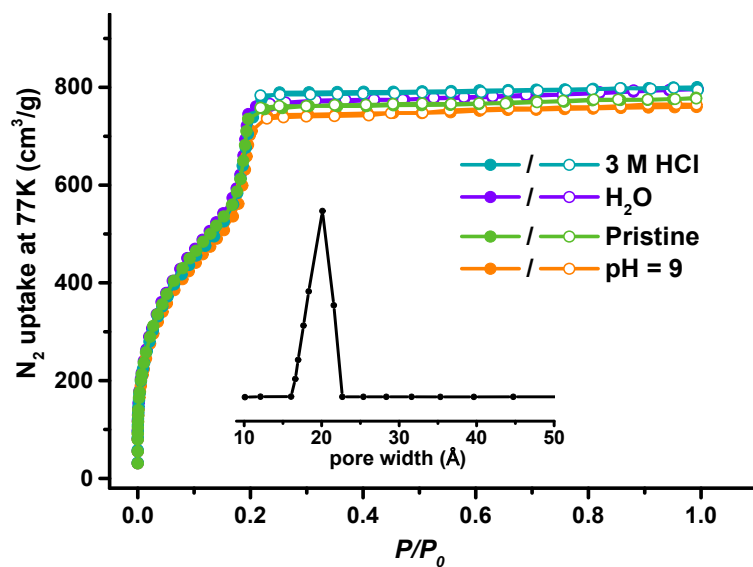


Figure S20. N₂ sorption isotherms of BUT-231 after treated in different solutions (inset shows pore size distribution evaluated from the N₂ adsorption data at 77 K).

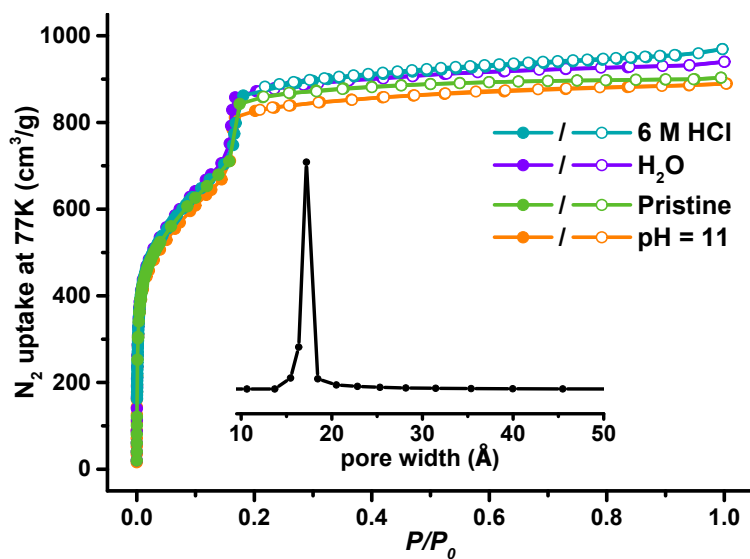


Figure S21. N₂ sorption isotherms of BUT-232 after treated in different solutions (inset shows pore size distribution evaluated from the N₂ adsorption data at 77 K).

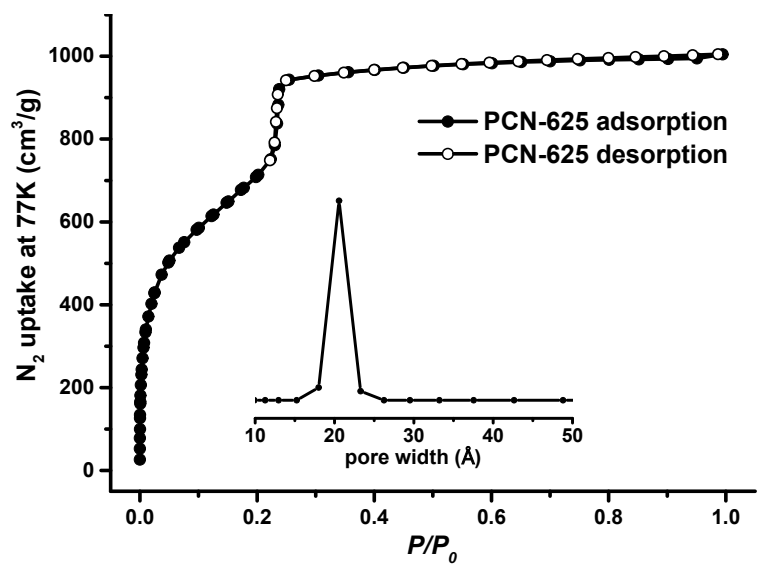


Figure S22. Nitrogen sorption isotherms of PCN-625 (inset shows pore size distribution evaluated from the N_2 adsorption data at 77 K).

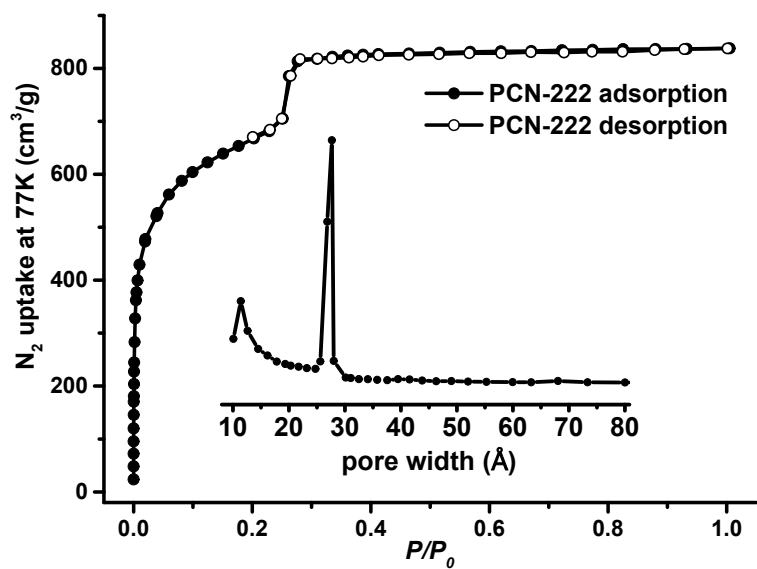


Figure S23. Nitrogen sorption isotherms of PCN-222 (inset shows pore size distribution evaluated from the N_2 adsorption data at 77 K).

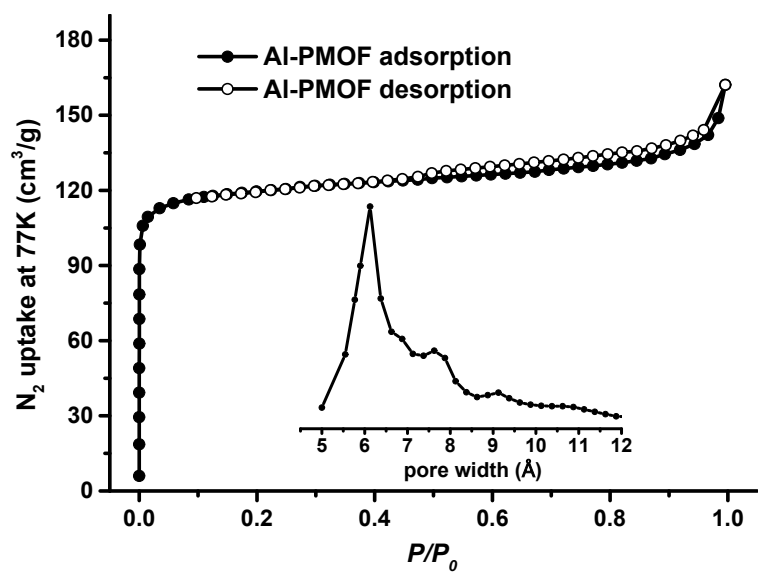


Figure S24. Nitrogen sorption isotherms of Al-PMOF (inset shows pore size distribution evaluated from the N₂ adsorption data at 77 K).

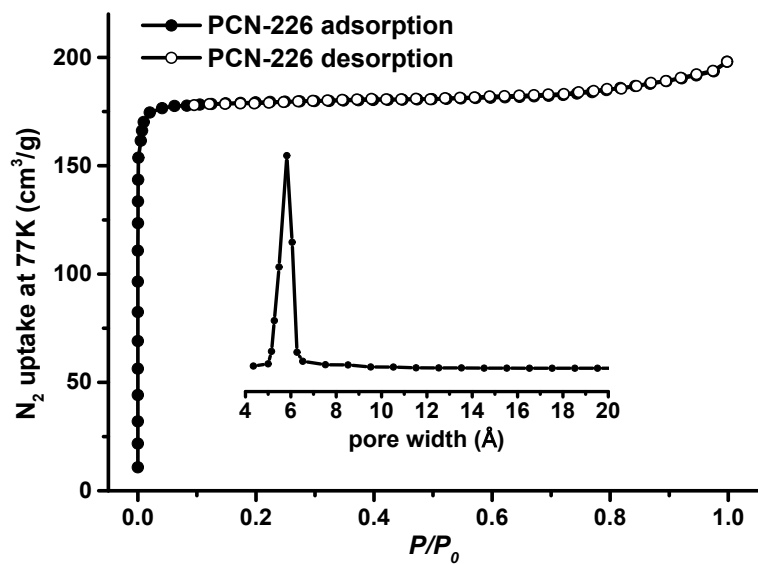


Figure S25. Nitrogen sorption isotherms of PCN-226 (inset shows pore size distribution evaluated from the N₂ adsorption data at 77 K).

S9. Thermogravimetric Analysis (TGA)

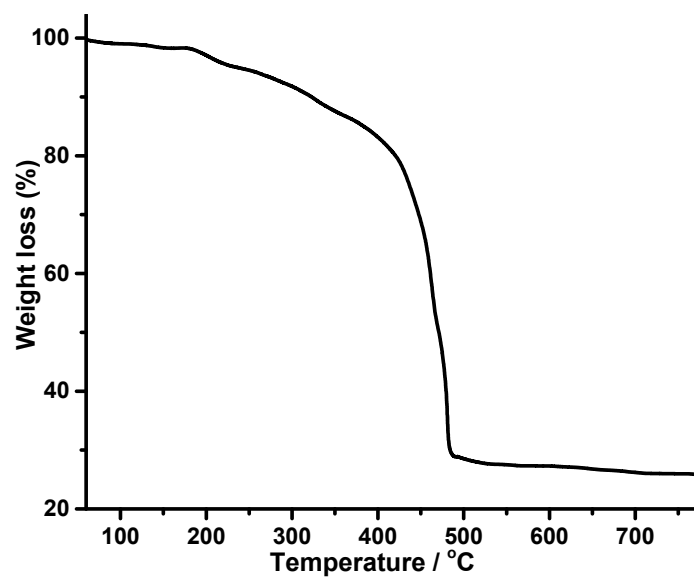


Figure S26. TGA curve of BUT-229.

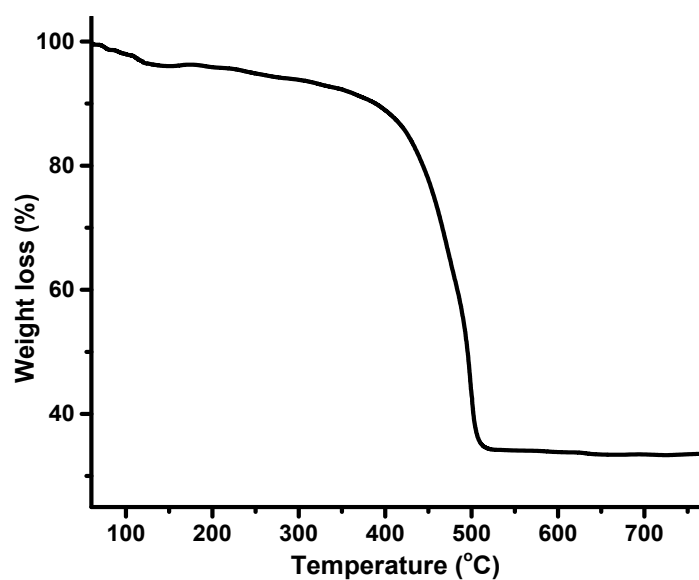


Figure S27. TGA curve of BUT-230.

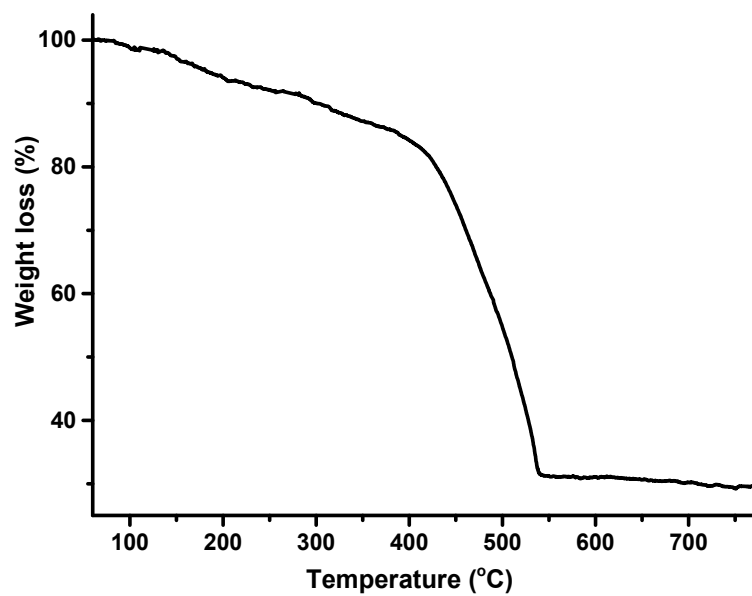


Figure S28. TGA curve of BUT-231.

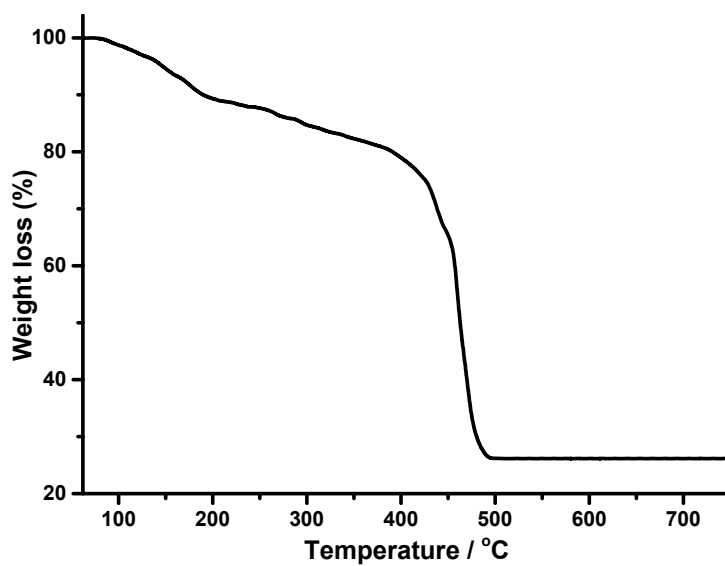


Figure S29. TGA curve of BUT-232.

S10. Fourier Transform Infrared Spectrometer Spectra (FT-IR)

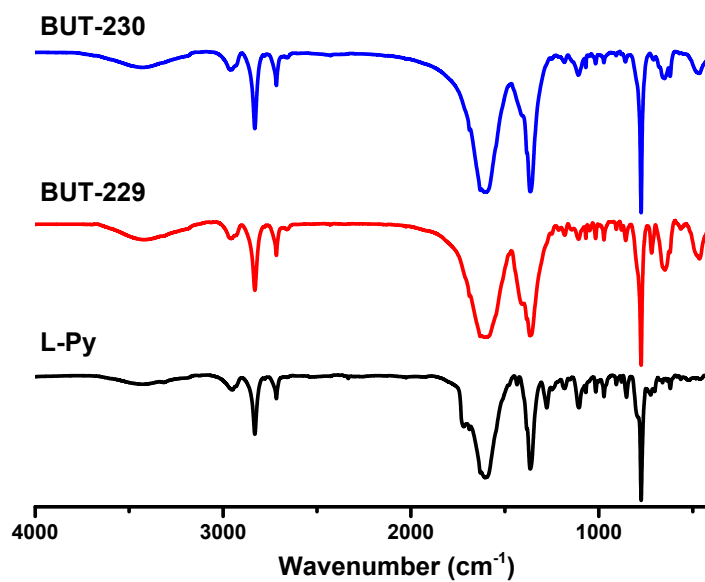


Figure S30. FT-IR spectra of L-Py, BUT-229, and BUT-230.

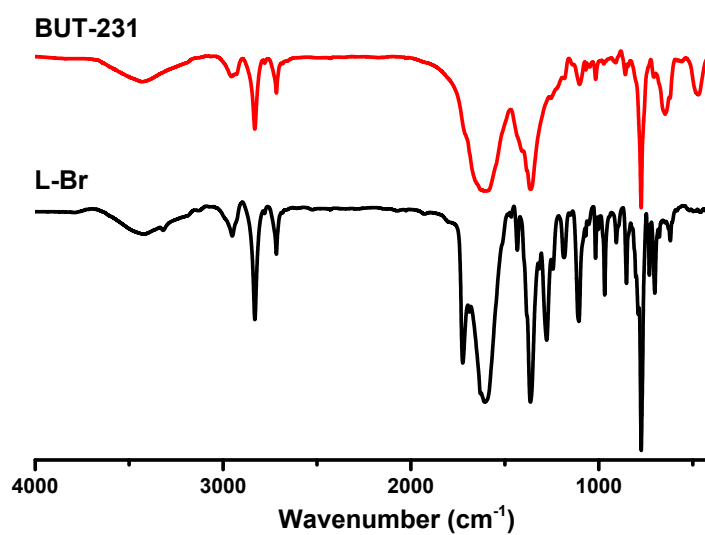


Figure S31. FT-IR spectra of L-Br and BUT-231.

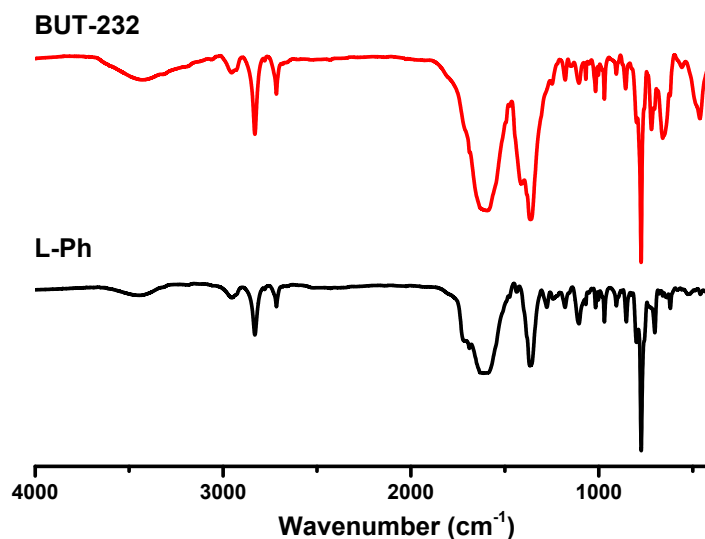


Figure S32. FT-IR spectra of L-Ph and BUT-232.

S11. Liquid-phase Adsorption

The BUT-229 or BUT-230 sample (15 mg) was transferred to a acetonitrile solution of benzyl alcohol with a given concentration (~10 mg/mL) in a vial. UV-vis spectra of the solutions were recorded (taking 100 μ L of sample and diluting with 3mL of acetonitrile) to characterize the adsorption performances of BUT-229/BUT-230 along with the soaking time at RT. The amounts of benzyl alcohol adsorbed on BUT-229/BUT-230 were calculated with the following equation:

$$Q_e = (C_0 - C_e)V/M \quad \text{Equation (S1)}$$

where Q_e (mg/g) is the equilibrium adsorbed amount, C_0 and C_e (mg/mL) are the initial and equilibrium concentrations of the solution, V (L) is the volume of the solution, and M (g) is the mass of the MOF. In order to ensure the accuracy of the measurements, all of the experiments were repeated at least three times, and the average values were reported. All materials were dried overnight under vacuum at 80 °C before each repeated use.

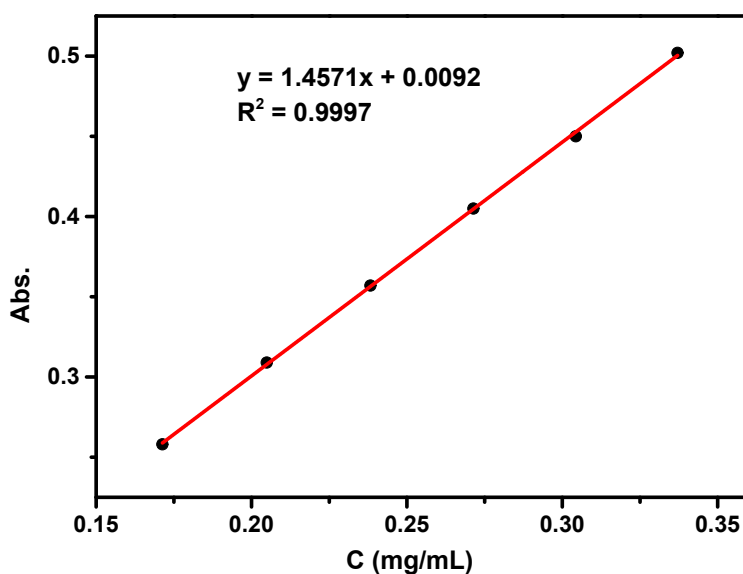


Figure S33. The standard curve between benzyl alcohol concentration and absorbance.

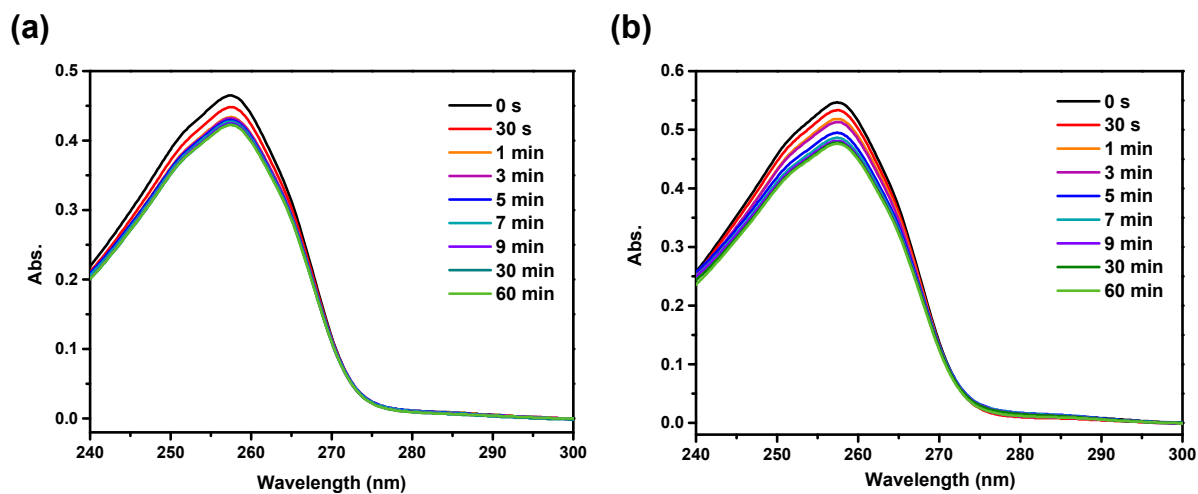


Figure S34. The UV-vis spectra of benzyl alcohol in acetonitrile during the adsorptions processed with (a) BUT-229 and (b) BUT-230 as adsorbents.

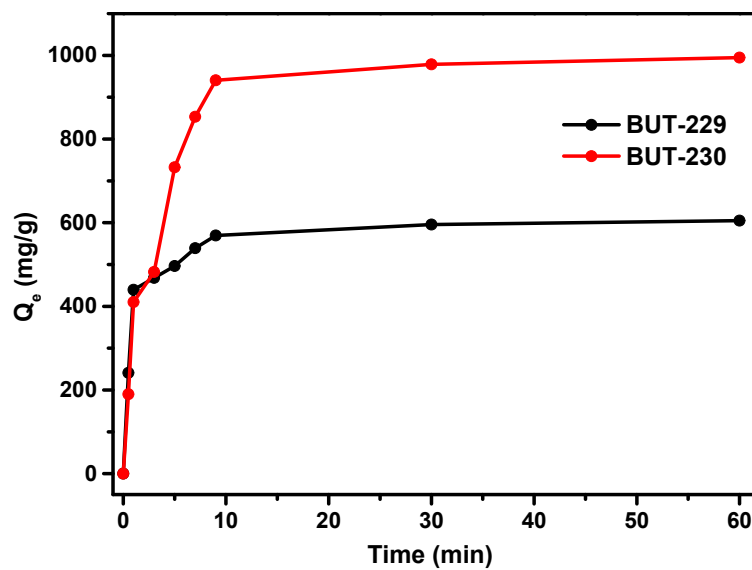


Figure S35. Benzyl alcohol adsorption kinetics of BUT-229 and BUT-230 in acetonitrile at 298 K.

S12. UV-vis/photoluminescence and electrochemical measurements

Tauc equation was utilized to calculate the band gap of the materials. The Tauc equation is as follows:

$$(\alpha h\nu)^{1/n} = A(h\nu - E_g)$$

Equation (S2)

Where E_g is the optical band gap, $h\nu$ is the energy of the incident photon, A is constant and α is the absorption coefficient. A value of $n = 1/2$ is used here for direct allowed transitions as the common practice for MOFs.⁷

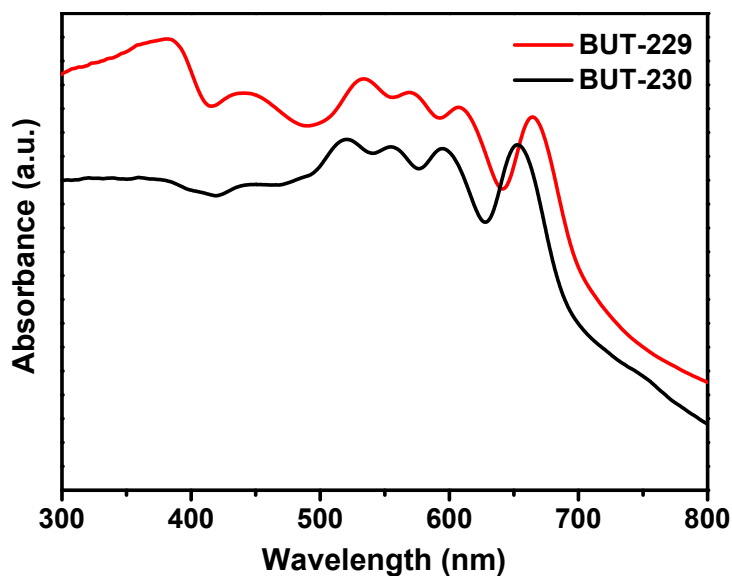


Figure S36. UV-vis diffuse reflectance spectra of BUT-229 and BUT-230.

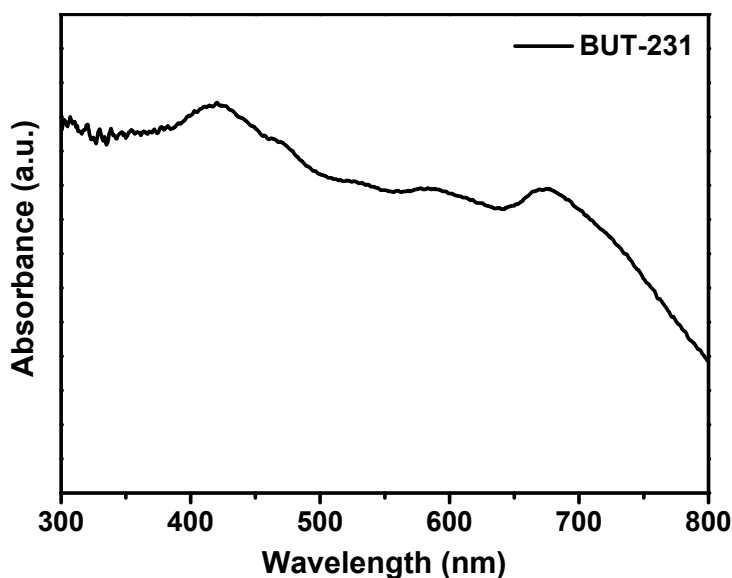


Figure S37. UV-vis diffuse reflectance spectra of BUT-231.

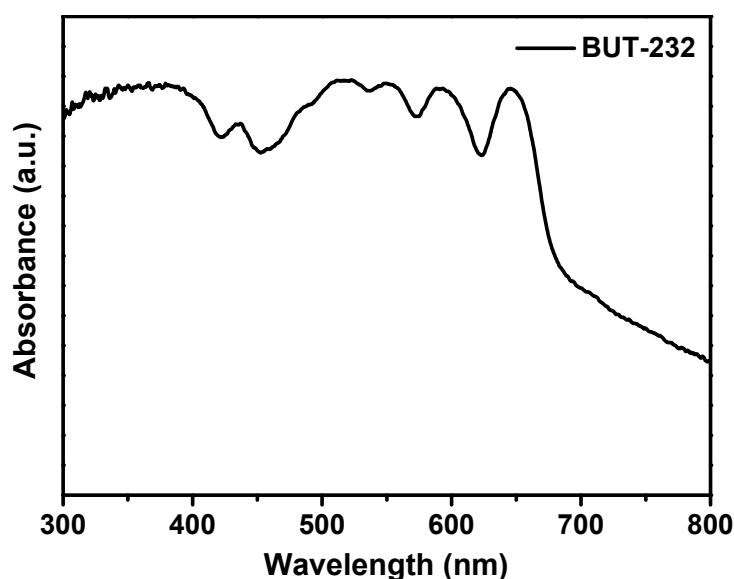


Figure S38. UV-vis diffuse reflectance spectra of BUT-232.

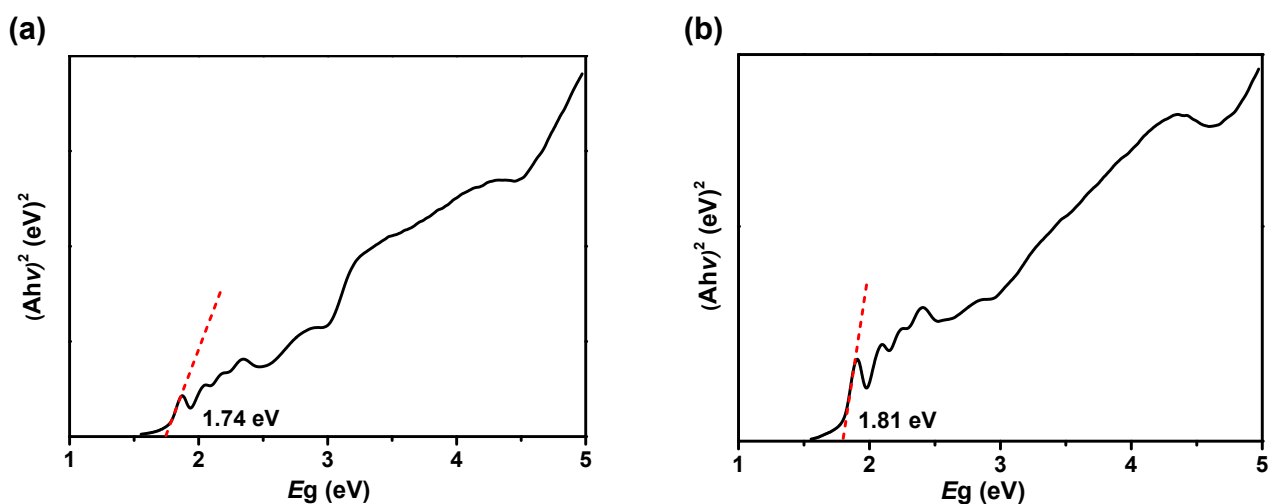


Figure S39. The Tauc plots of (a) BUT-229 and (b) BUT-230 for estimating the band gaps.

Mott-Schottky was carried out with a standard three-electrode system on a Zennium electrochemistry workstation at room temperature. Electrochemical impedance (EIS) and transient photocurrent responses were performed on a CHI 660E electrochemical workstation (Chenhua Instrument, Shanghai, China). All the electrolyte used in this work was 0.5 M Na_2SO_4 solution. The Pt plate and typical Ag/AgCl were chosen as the counter and reference electrodes, respectively. MOF-coated Fluorine-Tin-Oxide (FTO) glasses were as the working electrode. The MOF-coated electrode was fabricated as follows: 1 mg MOF was added into 2.0 mL ethanol and 50 μL Nafion mixed solution, sonicated for 30 min to afford a finely dispersed suspension. Then, 100 μL of the sample suspension was dropped onto the FTO plate ($1 \times 1 \text{ cm}^2$) and dried at room temperature for 30 min. The Mott-Schottky plots measurements were measured in the voltage range of $-0.8 \sim 1.0 \text{ V}$. The EIS was measured with a bias potential of -0.6 V over the frequency range of 10^{-2} to 10^5 Hz . The transient photocurrent response measurements of the samples were carried out under chopped light irradiation at 0.5 V . All the measured potential was converted with respect to normal hydrogen electrode (NHE) using the Nernst equation below:

$$E_{\text{NHE}} = E_{\text{Ag/AgCl}} + 0.2046. \quad \text{Equation (S3)}$$

Where E_{NHE} was the converted potential vs. NHE, $E_{\text{Ag/AgCl}}$ was the measured potential vs. Ag/AgCl electrode, and pH was 7.0 at $25 \text{ }^\circ\text{C}$.

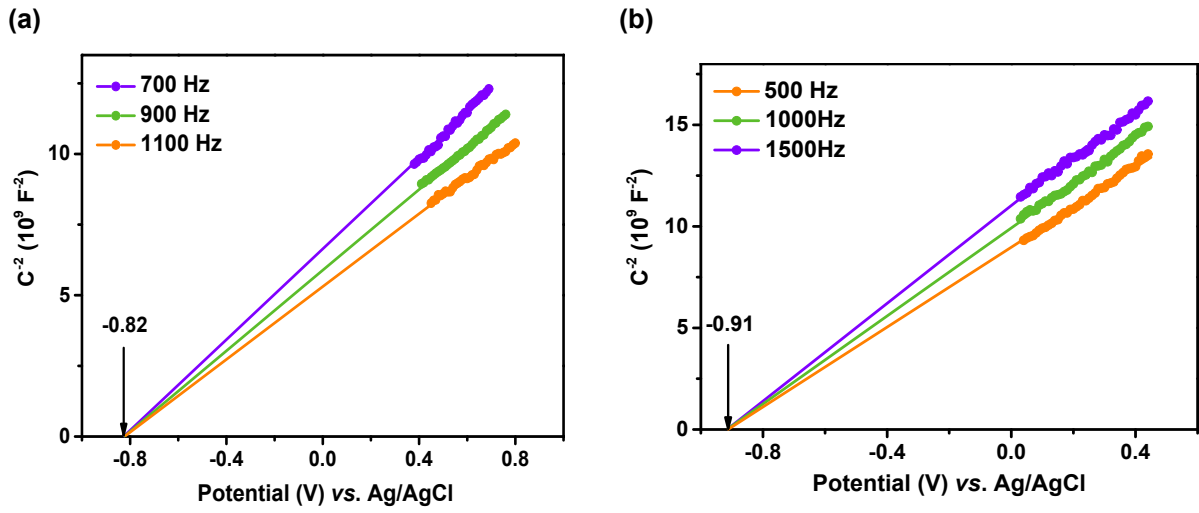


Figure S40. Mott-Schottky plots of (a) BUT-229 and (b) BUT-230.

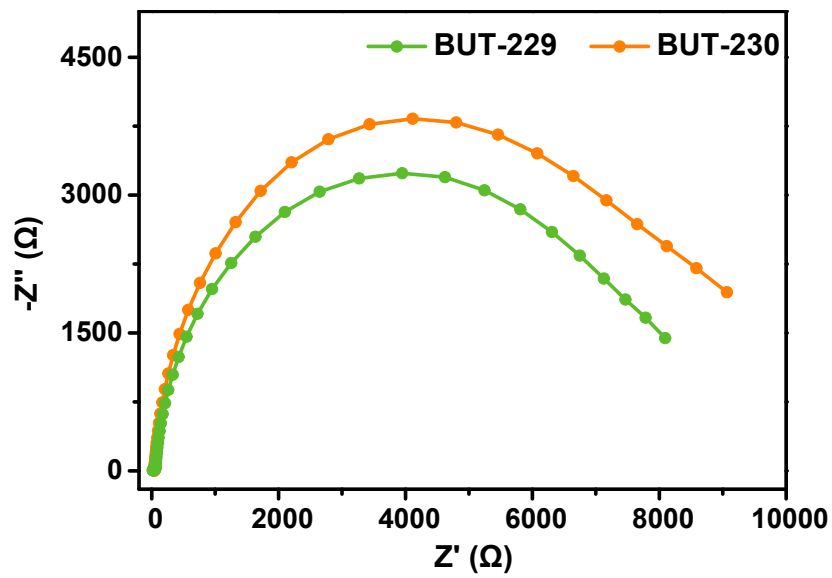


Figure S41. Electrochemical impedance spectra of BUT-229 and BUT-230.

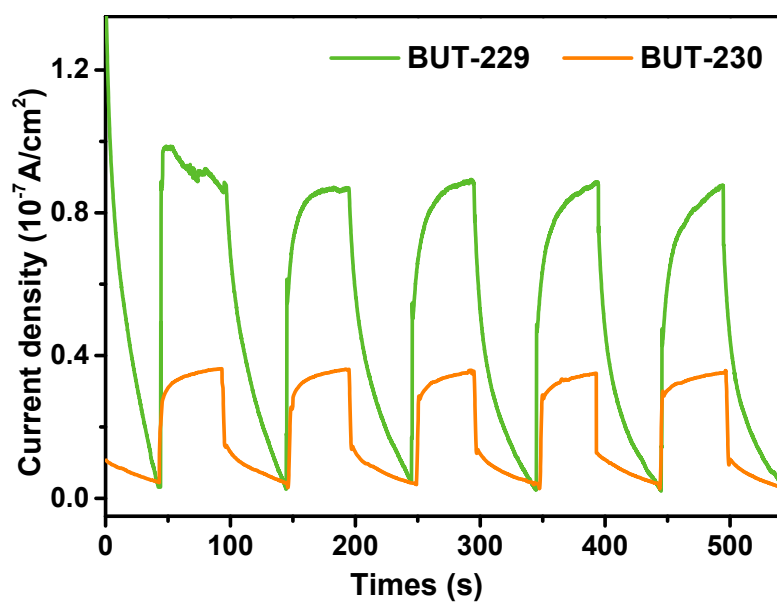


Figure S42. Transient photocurrent responses of BUT-229 and BUT-230.

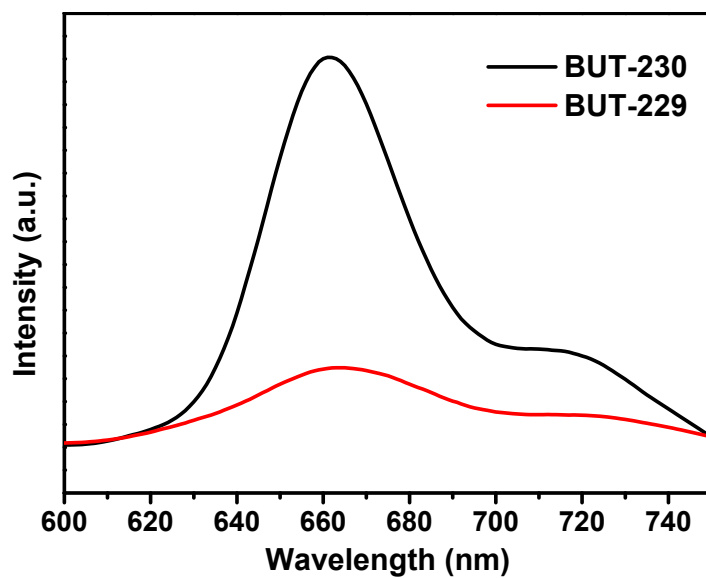


Figure S43. Steady-state photoluminescence spectra of BUT-229 and BUT-230.

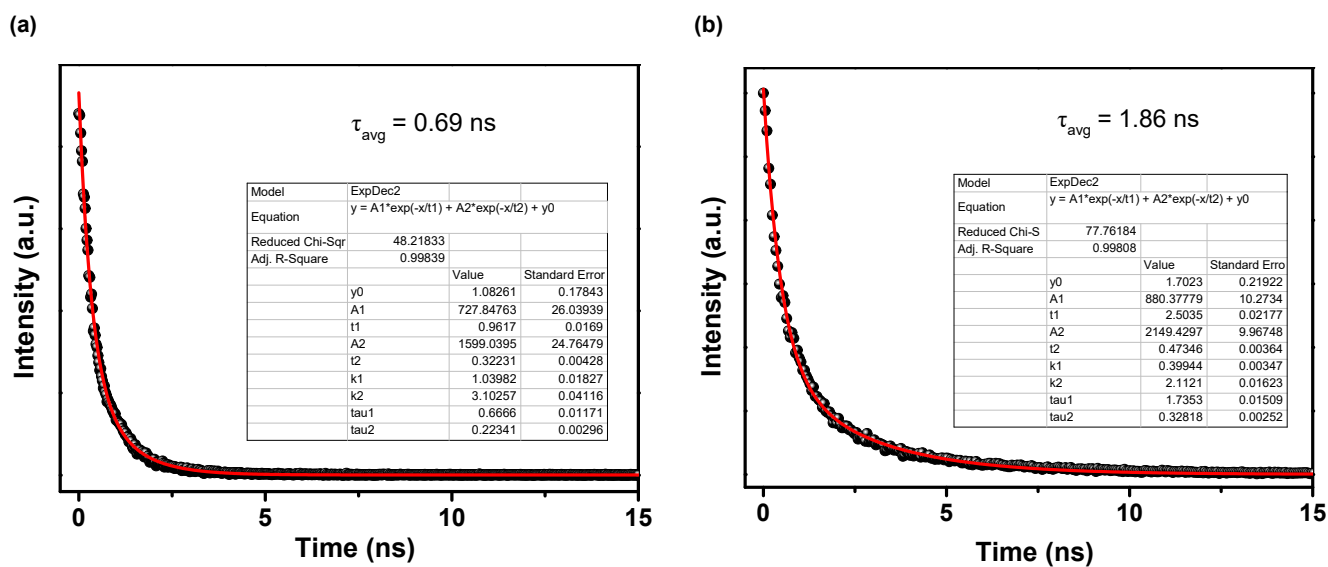
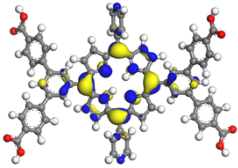
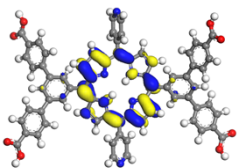
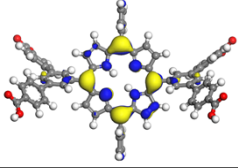
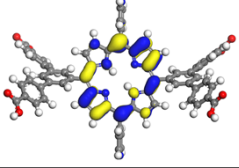


Figure S44. Time-resolved decay photoluminescence spectra of (a) BUT-229 and (b) BUT-230 (The average lifetime was calculated by using the equation: $\tau_{\text{avg}} = (A_1\tau_1^2 + A_2\tau_2^2)/(A_1\tau_1 + A_2\tau_2)$).

S13. DFT calculations for the HOMO and LUMO of ligands

Density functional theory (DFT) calculations : The molecular orbitals (HOMO and LUMO) of the ligand were calculated using the DMol3 module of Materials Studio. The generalized gradient approximation (GGA) with the Perdew-Burke-Ernzerhof (PBE) was used to describe the exchange-correlation interaction. The double numerical plus polarization (DNP) was used to expand electronic wave function. The self-consistent field (SCF) calculations were used and the convergence criterion is 10^{-5} Ha in energy. For accelerate SCF convergence, thermal smearing with a value of 0.01 Ha was used to orbital occupation.

Table S3. HOMO and LUMO of the L-Py ligand in different conformations obtained from DFT calculations.

Compound	HOMO	LUMO	Gap
A free L-Py ligand with the conformation as in BUT-229	-5.968 eV 	-4.320 eV 	1.648 eV
A free L-Py ligand with the conformation as in BUT-230	-5.981 eV 	-4.285 eV 	1.696 eV

S14. Electron Paramagnetic Resonance (EPR) Spectroscopy

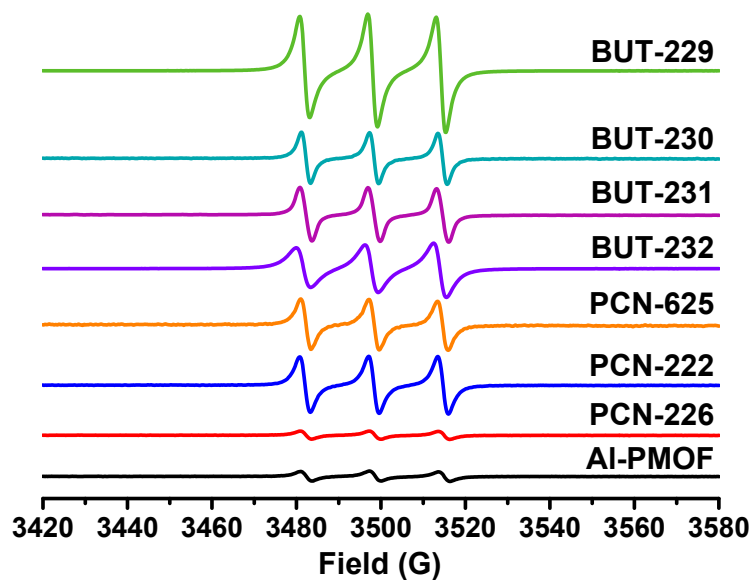


Figure S45. EPR spectra of BUT-229 to BUT-232 and other reported PMOF (PCN-625, PCN-222, PCN-226, Al-PMOF) in the irradiation by visible light in the presence of TEMP.

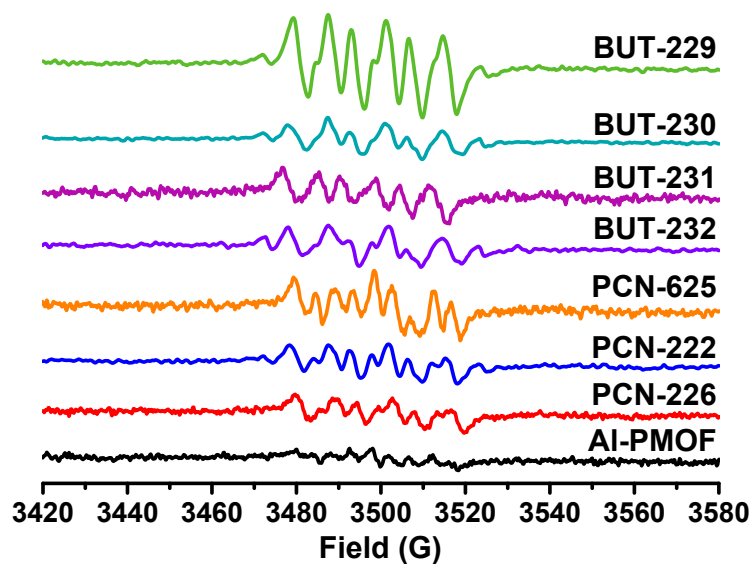


Figure S46. EPR spectra of BUT-229 to BUT-232 and other reported PMOF (PCN-625, PCN-222, PCN-226, Al-PMOF) in the irradiation by visible light in the presence of DMPO.

S15. Photocatalysis Data

Table S4. Oxidation of benzyl alcohol over different catalysts.

Entry	Catalyst	Topology	Yield (%)
1	BUT-229(Fe)	flu	74
2	BUT-230(Fe)	csq	26
3	BUT-229(Ni)	flu	62
4	BUT-230(Ni)	csq	21
5	BUT-229(Cu)	flu	50
6	BUT-230(Cu)	csq	18

Reaction condition: Catalyst (0.003 mmol), 2,2,6,6-tetramethylpiperidinoxy (TEMPO) (0.006 mmol), benzyl alcohol (0.1 mmol), CD₃CN (0.5 ml), visible LED light, O₂ balloon, lasting for 10 hours at room temperature. The metalloporphyrin ligands **M-L-Py** (M = Fe(III), Ni(II), Cu(II)) were synthesized according to procedure shown in Scheme S2.

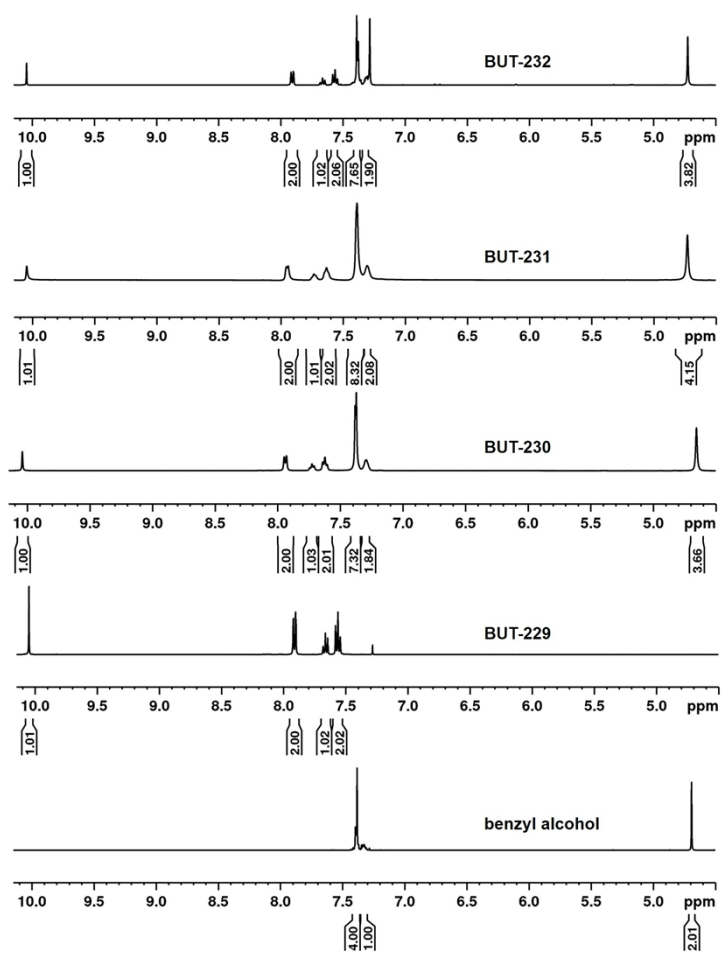


Figure S47. Monitoring of photocatalytic oxidation of benzyl alcohol to benzaldehyde by BUT-229-232 catalysts upon visible light irradiation at RT for 10 h.

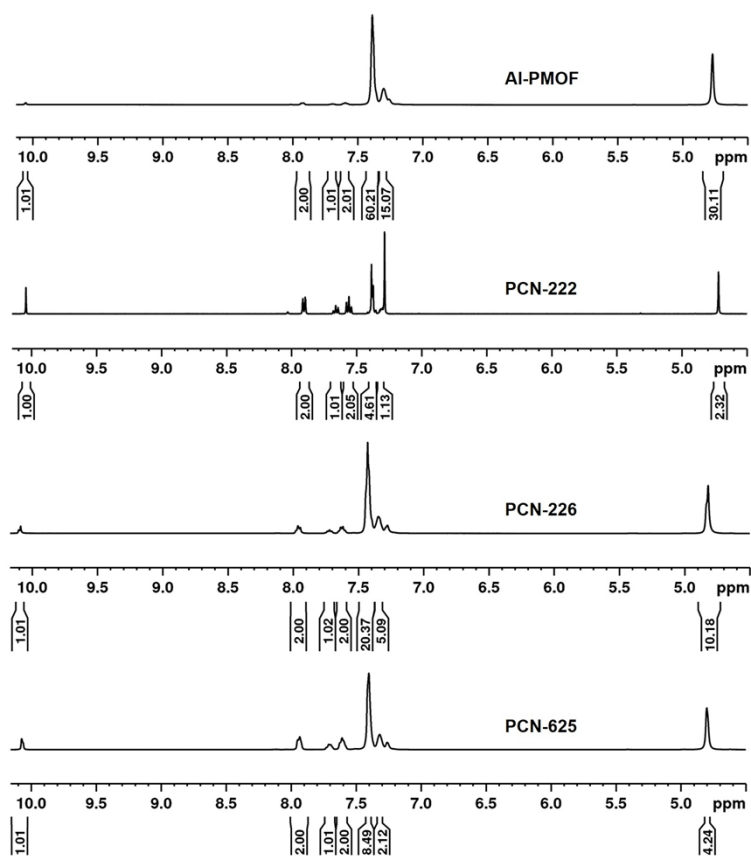


Figure S48. Monitoring of photocatalytic oxidation of benzyl alcohol to benzaldehyde by Al-PMOF, PCN-222, PCN-226, and PCN-625 catalysts upon visible light irradiation at RT for 10 h.

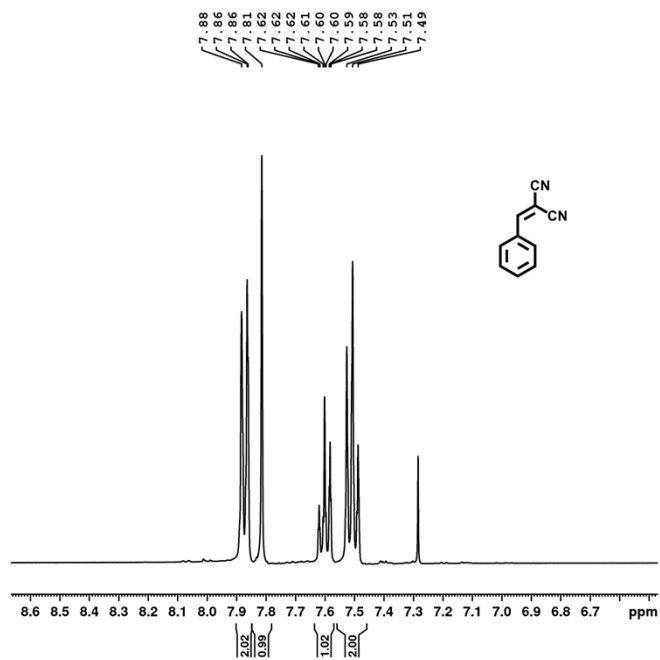


Figure S49. ^1H NMR (CDCl_3 , 400 MHz) spectrum of 2-benzylidenemalononitrile.

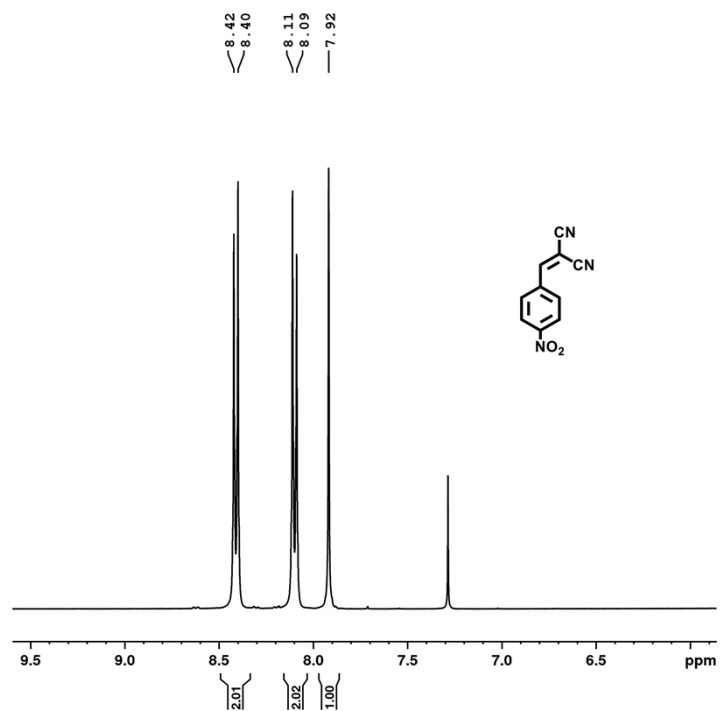


Figure S50. ^1H NMR (CDCl_3 , 400 MHz) spectrum of 2-(4-nitrobenzylidene)malononitrile.

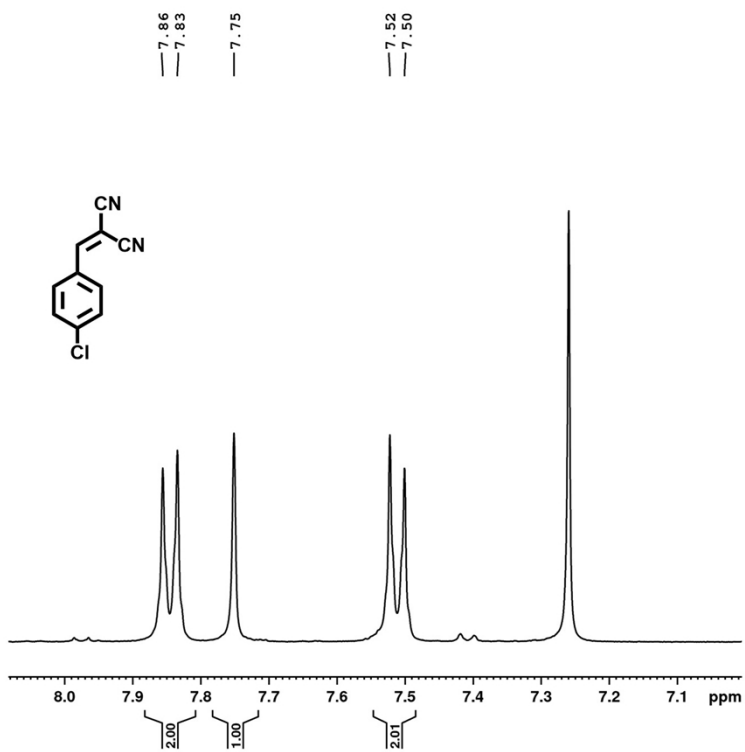


Figure S51. ^1H NMR (CDCl_3 , 400 MHz) spectrum of 2-(4-chlorobenzylidene)malononitrile.

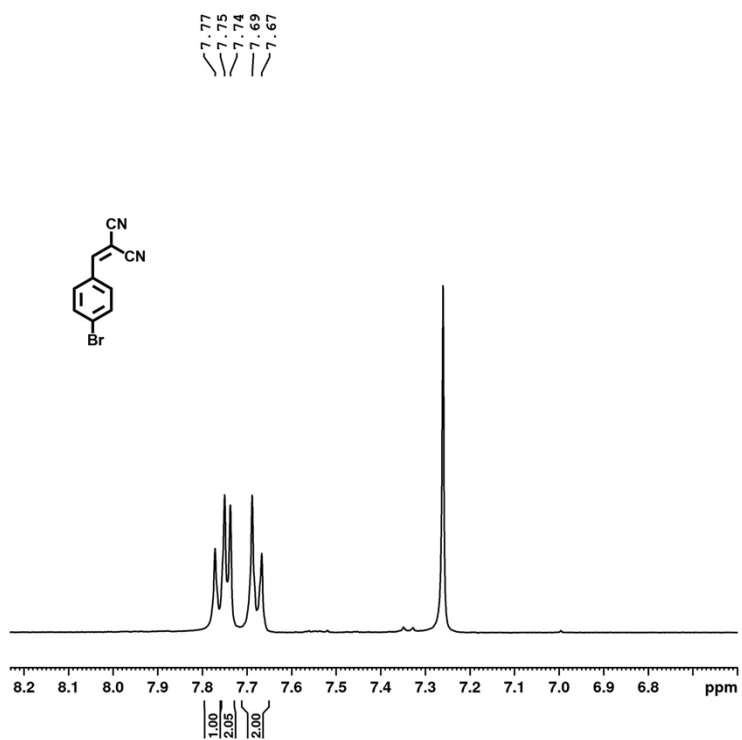


Figure S52. ^1H NMR (CDCl_3 , 400 MHz) spectrum of 2-(4-bromobenzylidene)malononitrile.

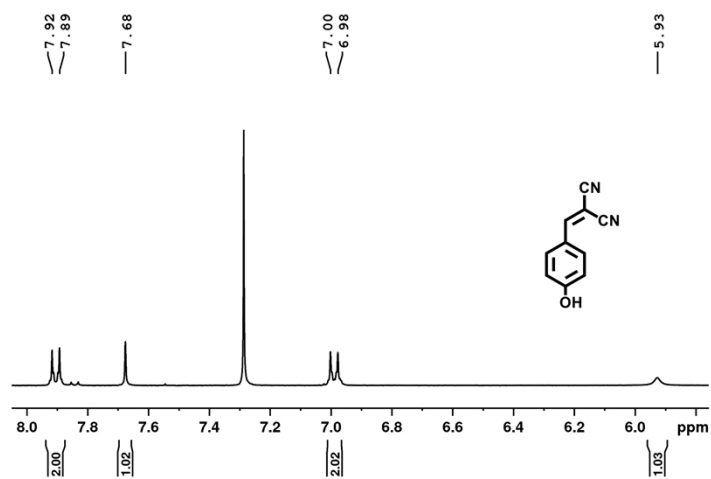


Figure S53. ^1H NMR (CDCl_3 , 400 MHz) spectrum of 2-(4-hydroxybenzylidene)malononitrile.

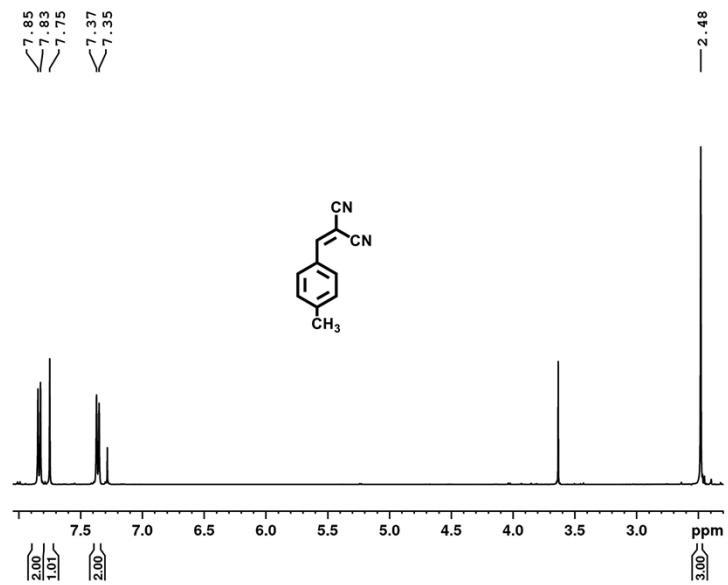


Figure S54. ^1H NMR (CDCl_3 , 400 MHz) spectrum of 2-(4-methylbenzylidene)malononitrile.

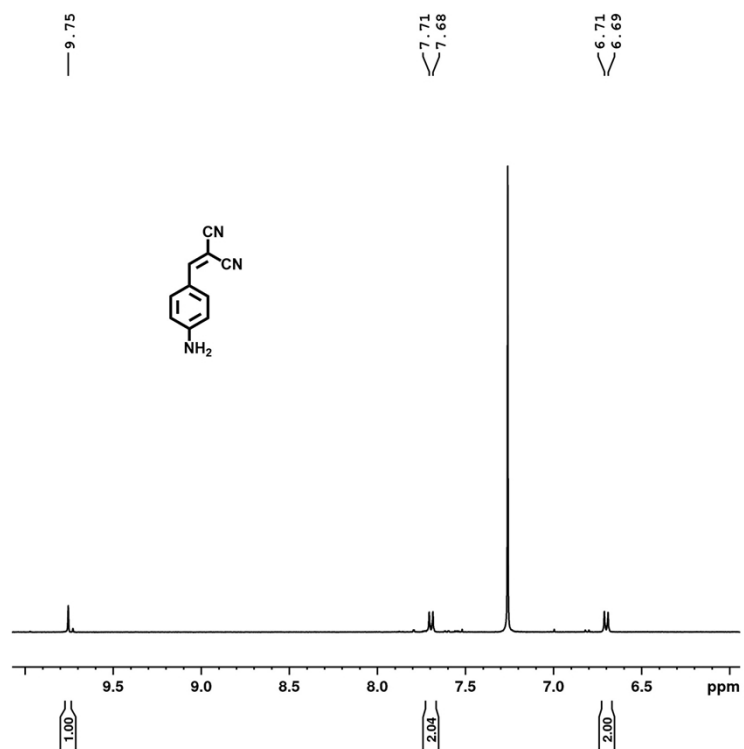


Figure S55. ^1H NMR (CDCl_3 , 400 MHz) spectrum of 2-(4-aminobenzylidene)malononitrile.

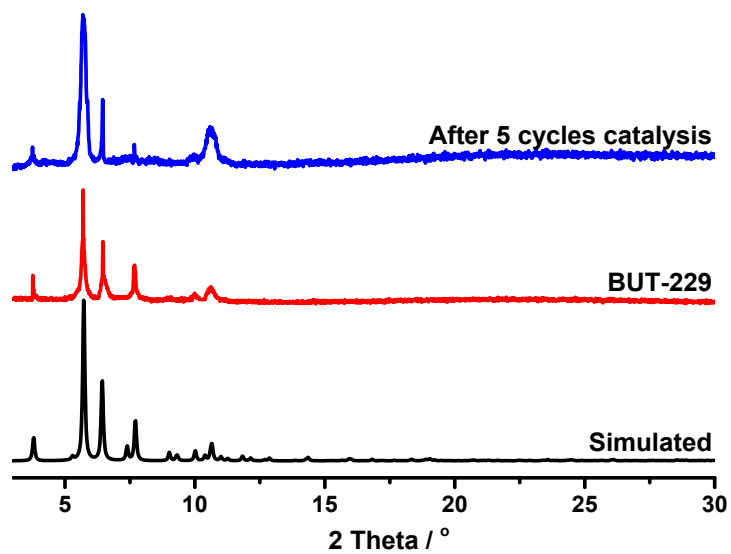


Figure S56. PXRD patterns of pristine BUT-229 and that after 5 catalytic cycles.

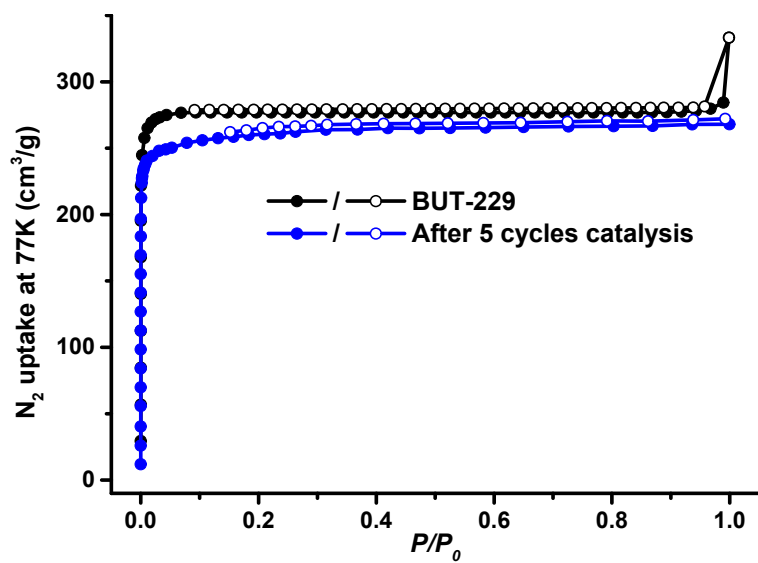


Figure S57. N_2 adsorption/desorption isotherms (at 77 K) of pristine BUT-229 and that after 5 catalytic cycles.

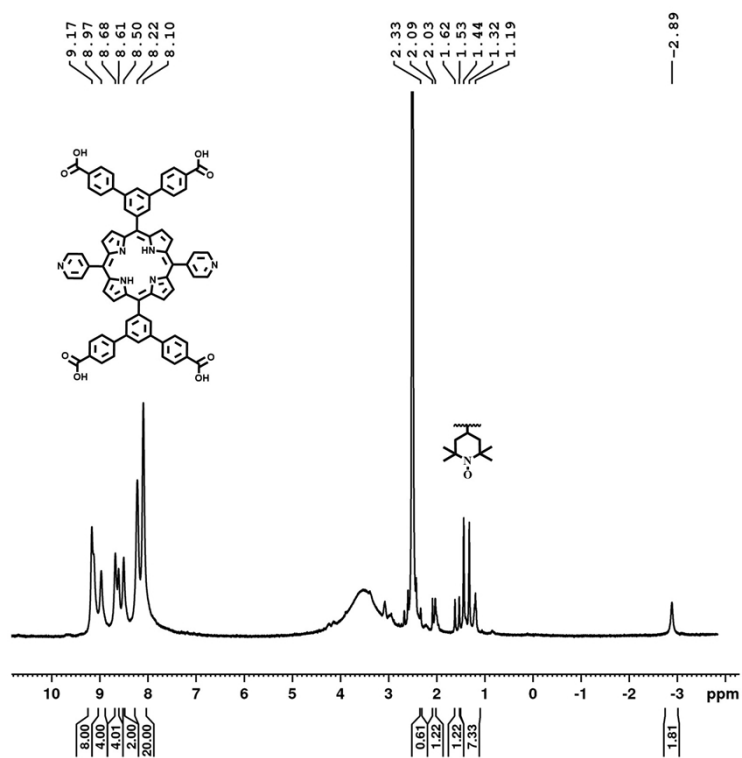


Figure S58. ^1H NMR ($\text{DMSO-}d_6$, 400 MHz) spectrum of the digested BUT-229-TEMPO.

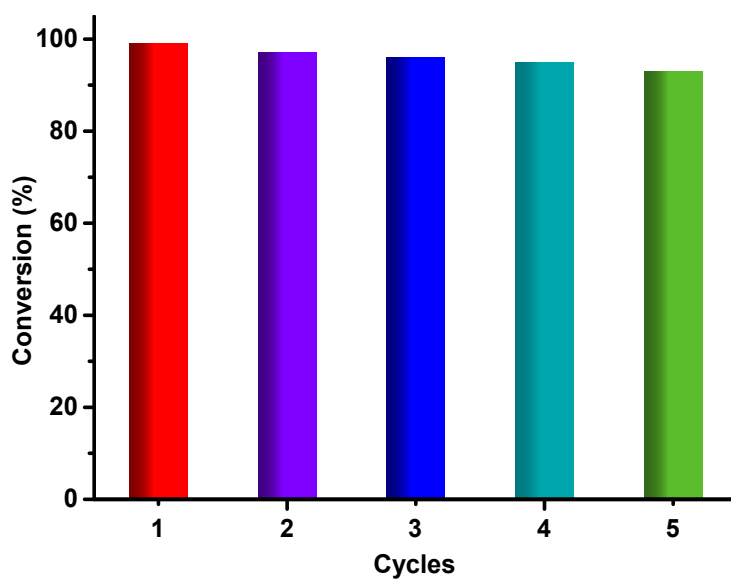


Figure S59. Catalytic efficiencies of BUT-229-TEMPO in five consecutive cyclic runs.

S16. References

1. W. Wu, Y. Xie, X.-L. Lv, L.-H. Xie, X. Zhang, T. He, G.-R. Si, K. Wang and J.-R. Li, Expanding the Structural Topologies of Rare-Earth Porphyrinic Metal-Organic Frameworks through Ligand Modulation, *ACS Appl. Mater. Interfaces*, 2023, **15**, 5357-5364.
2. S. Yuan, T. F. Liu, D. Feng, J. Tian, K. Wang, J. Qin, Q. Zhang, Y. P. Chen, M. Bosch, L. Zou, S. J. Teat, S. J. Dalgarno and H. C. Zhou, A Single Crystalline Porphyrinic Titanium Metal-Organic Framework, *Chem. Sci.*, 2015, **6**, 3926-3930.
3. L. Yang, P. Cai, L. Zhang, X. Xu, A. A. Yakovenko, Q. Wang, J. Pang, S. Yuan, X. Zou, N. Huang, Z. Huang and H.-C. Zhou, Ligand-Directed Conformational Control over Porphyrinic Zirconium Metal-Organic Frameworks for Size-Selective Catalysis, *J. Am. Chem. Soc.*, 2021, **143**, 12129-12137.
4. X. Gong, Y. Shu, Z. Jiang, L. Lu, X. Xu, C. Wang and H. Deng, Metal-Organic Frameworks for the Exploitation of Distance between Active Sites in Efficient Photocatalysis, *Angew. Chem. Int. Ed.*, 2020, **59**, 5326-5331.
5. M. O. Cichocka, Z. Liang, D. Feng, S. Back, S. Siahrostami, X. Wang, L. Samperisi, Y. Sun, H. Xu, N. Hedin, H. Zheng, X. Zou, H.-C. Zhou and Z. Huang, A Porphyrinic Zirconium Metal-Organic Framework for Oxygen Reduction Reaction: Tailoring the Spacing between Active-Sites through Chain-Based Inorganic Building Units, *J. Am. Chem. Soc.*, 2020, **142**, 15386-15395.
6. A. Fateeva, P. A. Chater, C. P. Ireland, A. A. Tahir, Y. Z. Khimyak, P. V. Wiper, J. R. Darwent and M. J. Rosseinsky, A Water-Stable Porphyrin-based Metal-Organic Framework Active for Visible-Light Photocatalysis, *Angew. Chem. Int. Ed.*, 2012, **51**, 7440-7444.
7. H.-Q. Xu, J. Hu, D. Wang, Z. Li, Q. Zhang, Y. Luo, S.-H. Yu and H.-L. Jiang, Visible-Light Photoreduction of CO₂ in a Metal-Organic Framework: Boosting Electron-Hole Separation via Electron Trap States, *J. Am. Chem. Soc.*, 2015, **137**, 13440-13443.